Commun Nonlinear Sci Numer Simulat 142 (2025) 108550

Contents lists available at ScienceDirect

Communications in Nonlinear Science and Numerical Simulation

journal homepage: www.elsevier.com/locate/cnsns

Research paper

Semi-analytical attitude propagation of low-altitude Earth orbiting objects

I. Cavallari, J. Feng, M. Vasile *

Aerospace Centre of Excellence, University of Strathclyde, 75 Montrose Street, G11XJ, Glasgow, UK

ARTICLE INFO

Keywords:
Attitude dynamics
Semi-analytical theory
Atmospheric drag
Astrodynamics

ABSTRACT

The paper introduces an averaged model suitable for studying the long-term attitude dynamics of low Earth orbit objects subject to the interaction with the exosphere. This work extends previous results by the authors on the development of a semi-analytical theory for long-term attitude propagation. The first-order averaged model is developed by expressing the rotational problem in modified Sadov variables and performing the average of the equations of motion over the fast Sadov angles and the orbital mean anomaly. A transformation from osculating to mean variables is also derived from a combination of Lie transformations. The approach proposed in this paper is applied to two possible atmospheric drag models: a simple, commonly used, model characterised by a constant dimensionless drag coefficient and a higher fidelity model based on the theory by Sentman (1961).

1. Introduction

This paper is an extension of previous work by the authors [1], where we proposed a semi-analytical theory suitable to study the long-term attitude dynamics of Earth-orbiting objects subject to the effects of gravity gradient, residual magnetic, and light pressure torques. While the semi-analytical theory developed in [1] is appropriate to study the attitude motion of objects in medium and high altitude orbits, it is incomplete for low altitude orbits, where the effects of atmospheric drag is not negligible. In this work, we present a method to integrate the torques, induced by atmospheric forces, into the averaged model.

In the literature on analytical and semi-analytical theories for the attitude dynamics of space objects one can find the works by Ferrandiz and Sansaturio [2], Vallejo [3], Elipe and Vallejo [4], Lara and Ferrer [5], Lara [6], dealing with the dynamics of triaxial satellites affected by the gravity-gradient torque, and the work by Sidorenko [7], Zanardi and Vilhena de Moraes [8], Celletti and Sidorenko [9], Garcia et al. [10], Mohmmed et al. [11], Efimov et al. [12], Benson and Scheeres [13,14], on the long-term attitude dynamics of artificial Earth orbiting objects. However, only a limited body of works exists on analytical and semi-analytical theories for the study of the long-term attitude dynamics of space objects affected by atmospheric forces. The most known works are those by Zanardi et al. [15,16,17], Zanardi et al. [18], who developed and analysed an analytical solution for the evolution of the spin velocity and axis. Their theory was applied to and validated for the two Brazilian satellites SCD1 and SCD2. Also Ray and Scheeres [19] developed a semi-analytical theory for the coupled orbital and attitude dynamics affected by atmospheric drag. However, they have the specific purpose of predicting the long-term orbital dynamics and do not focus on the long-term propagation of the attitude motion.

In this paper, we develop a first-order averaged attitude model suitable for both triaxial and axisymmetric objects subject to atmospheric forces. This is obtained by expressing the attitude problem in the modified Sadov variables introduced in [see

* Corresponding author.
E-mail address: massimiliano.vasile@strath.ac.uk (M. Vasile).

https://doi.org/10.1016/j.cnsns.2024.108550
Received 23 May 2024; Received in revised form 13 December 2024; Accepted 13 December 2024
Available online 19 December 2024
1007-5704/© 2024 The Authors. Published by Elsevier B.V. This is an open access article under the CC BY license (http://creativecommons.org/licenses/by/4.0/).

1] and averaging the equations of motion over the fast Sadov angles and the orbital mean anomaly. The averaging is partially performed numerically to handle different kinds of force and atmospheric models. This approach makes it complex to compute the transformation from osculating to mean modified Sadov variables, required to increase the accuracy of the semi-analytical solution. In line with the previous work by the authors [1], we compute the transformation as a combination of Lie transformations [see 20]. The generators of the Lie transformations are estimated by combining the method suggested by Elipe and Vallejo [4], Vallejo [3] and numerical methods.

In the literature on the attitude motion of space objects, one can find different models of atmospheric forces. The classical model used, for instance, by Beletsky [21], Zanardi et al. [15,16] assumes a constant dimensionless drag coefficient. Other models include a more detailed description of gas-surface interaction [see 22–24]. The technique proposed in this paper is applicable to all models that do not present any kind of discontinuity. As an example we will derive a semi-analytical solution for both the model proposed by Beletsky [21], Zanardi et al. [15,16] and for a more complex model, based on the theory by Sentman [25]. In the remainder of the paper we will call the model by Beletsky [21], *low-fidelity model*, and the one by Sentman [25], *mid-fidelity model*. The results in the paper demonstrate that the difference between the semi-analytical and numerical solutions is comparable for both the low-fidelity and mid-fidelity models. Furthermore, we will show that the mid-fidelity model presents features in the evolution of the dynamics that are not captured by the low-fidelity model.

The paper is organised as follows. In Section 2, we revise the definition of the modified Sadov variables. In Section 4 we describe in details the two atmospheric drag models considered in this work. Sections 4–6 are about the determination of the averaged model, the transformation from osculating to mean variables and the coupling between the attitude and orbital dynamics. Finally, Sections 7 and 8 describe numerical simulations and analysis used to assess the accuracy of the averaged model and its discrepancy with respect to the full non-averaged attitude dynamics.

2. Modified Sadov variables

We express the attitude problem in the modified Sadov variables $\boldsymbol{s} = (\zeta, J_g, J_h, \psi_l, \psi_g, \psi_h)$ introduced in [1]. We recall that the Sadov variables are action–angle variables for the torque-free rotational problem, derived from a canonical transformation of the Andoyer–Serret variables [see 4,5]. Unlike the latter, not all the Sadov variables have a straightforward physical meaning. Consider a fixed-axes reference frame $OXYZ$ and a rotating reference frame $Oxyz$ with principal axes of inertia, both centred in the satellite's centre of mass. Let (A, B, C) be the principal moments of inertia:

$$A = \int (y^2 + z^2)\mathrm{d}m, \quad B = \int (x^2 + z^2)\mathrm{d}m, \quad C = \int (x^2 + y^2)\mathrm{d}m,$$

with $\mathrm{d}m$ the mass element. The variable ζ is related to the satellite's distribution of mass and its rotational kinetic energy T_k:

$$\zeta = \frac{C(J_d - A)}{J_d(C - A)}$$

where

$$J_d = \frac{J_g^2}{2T_k} \tag{1}$$

is the satellite's dynamic moment. The Sadov actions J_g and J_h correspond to the magnitude of the angular momentum $\boldsymbol{G}$ and its projection on the Z axis, respectively. The angle ψ_h is defined between the X axis and $\hat{e}_{iG}$, i.e. the unit vector identifying the intersection between the OXY plane and the plane γ perpendicular to $\boldsymbol{G}$ (see Fig. 1). Setting

$$\kappa = \frac{C}{A}\frac{B - A}{C - B}, \quad \mu = \frac{1 - \zeta}{\zeta}\kappa, \tag{2}$$

the remaining angles are defined as

$$\psi_l = \frac{\pi}{2}\frac{F(\lambda, \mu)}{K(\mu)},$$
$$\psi_g = g + \sqrt{\frac{1 + \kappa}{\zeta}}\left(\Pi(-\kappa, \lambda, m) - \frac{\Pi(-\kappa, \mu)}{K(\mu)}F(\lambda, \mu)\right),$$

where $F(\lambda, \mu)$ is the incomplete integral of first kind with parameter μ, $\Pi(-\kappa, \lambda, \mu)$ is the incomplete integral of third kind with characteristic $-\kappa$ and parameter μ, and

$$K(\mu) = F(\pi/2, \mu), \quad \Pi(-\kappa, \mu) = \Pi(-\kappa, \pi/2, \mu),$$

[see 26]. In the above equations, g is the angle between $\hat{e}_{iG}$ and $\hat{e}_{bG}$, identifying the intersection between the planes γ and Oxy (see Fig. 1). Instead, λ is related to the angle l defined between $\hat{e}_{bG}$ and the x axis (see Fig. 1):

$$\sin\lambda = -\frac{\cos l}{\sqrt{1 + \kappa\sin^2 l}}, \quad \cos\lambda = \frac{\sqrt{1 + \kappa}\sin l}{\sqrt{1 + \kappa\sin^2 l}}.$$

If we replace ζ with the action J_l conjugated to the angle ψ_l, defined as

$$J_l = \frac{2J_g}{\pi}\sqrt{\frac{1 + \kappa}{\zeta}}\left(\Pi(-\kappa, \mu) - (1 - \zeta)K(\mu)\right),$$

we obtain the original set of Sadov variables [see 5].

The choice of the rotating reference frame is not arbitrary. It should be defined so that $\kappa > 0$ and $\mu \in [0, 1]$. Thus, if the satellite is rotating in a short axis mode (*SAM*), the rotating frame has to be selected so that $A < B < C$; on the contrary, if the satellite is in a long axis mode (*LAM*), $Oxyz$ must be such that $A > B > C$. Once selected the suitable reference frame, the rotation matrix from $OXYZ$ to $Oxyz$ is

$$\mathbf{R}_{\mathrm{i2b}} = \mathbf{R}_b \mathbf{R}_\delta \mathbf{R}_h, \tag{3}$$

with

$$\mathbf{R}_h = \begin{bmatrix} \cos\psi_h & \sin\psi_h & 0 \\ -\sin\psi_h & \cos\psi_h & 0 \\ 0 & 0 & 1 \end{bmatrix}, \quad \mathbf{R}_\delta = \begin{bmatrix} 1 & 0 & 0 \\ 0 & \frac{J_h}{J_g} & \sqrt{1-\frac{J_h^2}{J_g^2}} \\ 0 & -\sqrt{1-\frac{J_h^2}{J_g^2}} & \frac{J_h}{J_g} \end{bmatrix},$$

and $\mathbf{R}_b$ a matrix of elements b_{ij}, $i = 1..3$, $j = 1..3$, equal to

$$b_{11} = -\left(\sqrt{\zeta}\sin\left(\psi_g + \delta g\right)\mathrm{cn}(u,\mu)\mathrm{dn}(u,\mu) + \sqrt{1+\kappa}\cos\left(\psi_g + \delta g\right)\mathrm{sn}(u,\mu)\right) dnk^{-\frac{1}{2}}, \tag{4}$$

$$b_{12} = -\left(\sqrt{1+\kappa}\sin\left(\psi_g + \delta g\right)\mathrm{sn}(u,\mu) - \sqrt{\zeta}\cos\left(\psi_g + \delta g\right)\mathrm{dn}(u,\mu)\mathrm{cn}(u,\mu)\right) dnk^{-\frac{1}{2}}, \tag{5}$$

$$b_{13} = \sqrt{1-\zeta}\,\mathrm{cn}(u,\mu), \tag{6}$$

$$b_{21} = -\left(\cos\left(\psi_g + \delta g\right)\mathrm{cn}(u,\mu) - \sqrt{1+\kappa}\sqrt{\zeta}\sin\left(\psi_g + \delta g\right)\mathrm{sn}(u,\mu)\,\mathrm{dn}(u,\mu)\right) dnk^{-\frac{1}{2}}, \tag{7}$$

$$b_{22} = -\left(\sqrt{1+\kappa}\sqrt{\zeta}\cos\left(\psi_g + \delta g\right)\mathrm{sn}(u,\mu)\,\mathrm{dn}(u,\mu) + \sin\left(\psi_g + \delta g\right)\mathrm{cn}(u,\mu)\right) dnk^{-\frac{1}{2}}, \tag{8}$$

$$b_{23} = -\sqrt{1-\zeta}\sqrt{1+\kappa}\,\mathrm{sn}(u,\mu), \tag{9}$$

$$b_{31} = \sqrt{1-\zeta}\sin\left(\psi_g + \delta g\right) dnk^{\frac{1}{2}}, \tag{10}$$

$$b_{32} = -\sqrt{1-\zeta}\cos\left(\psi_g + \delta g\right) dnk^{\frac{1}{2}}, \tag{11}$$

$$b_{33} = \sqrt{\zeta}\,\mathrm{dn}(u,\mu), \tag{12}$$

[see 1]. In the above equations, $\mathrm{cn}(u,\mu)$ is the Jacobi elliptic cosine, $\mathrm{sn}(u,\mu)$ is the Jacobi elliptic sine, $\mathrm{dn}(u,\mu)$ is the Jacobi elliptic delta amplitude [see 27], and

$$\delta g = -\sqrt{\frac{1+\kappa}{\zeta}}\left(\Pi(-\kappa,\lambda,\mu) - u\frac{\Pi(-\kappa,\mu)}{K(\mu)}\right), \quad dnk = 1 + \kappa\,\mathrm{sn}^2(u,\mu), \quad u = \frac{2K(\mu)\psi_l}{\pi}.$$

When the satellite's rotation is affected by an external torque $\boldsymbol{M}$ the attitude equations of motion are

$$\frac{\mathrm{d}\boldsymbol{s}}{\mathrm{d}t} = \mathbf{A}\nabla_s \boldsymbol{\Phi} + \mathbf{B}\boldsymbol{M}, \tag{13}$$

where $\boldsymbol{\Phi}$ is the torque-free Hamiltonian [see 5], namely

$$\boldsymbol{\Phi} = \frac{J_g^2}{2AC}\left(A\zeta + C(1-\zeta)\right), \tag{14}$$

∇_s is the gradient operator, and [see 1]

$$\mathbf{A} = \begin{bmatrix} 0 & \tilde{\mathbf{I}} \\ -\tilde{\mathbf{I}}^{\mathrm{T}} & 0 \end{bmatrix}, \quad \tilde{\mathbf{I}} = \begin{bmatrix} -\frac{\pi}{J_g K(\mu)}\sqrt{\frac{\zeta}{1+\kappa}} & \frac{2(\Pi(-\kappa,\mu)-(1-\zeta)K(\mu))}{J_g K(\mu)} & 0 \\ 0 & -1 & 0 \\ 0 & 0 & -1 \end{bmatrix}, \tag{15}$$

$$\mathbf{B} = \begin{bmatrix} -\frac{2\zeta}{J_g}b_{13} & -\frac{2\zeta(1-\mu)}{J_g(1+\kappa)}b_{23} & \frac{2(1-\zeta)}{J_g}b_{33} \\ b_{13} & b_{23} & b_{33} \\ \frac{b_{13}J_h + b_{12}\sqrt{J_g^2-J_h^2}}{J_g} & \frac{b_{23}J_h + b_{22}\sqrt{J_g^2-J_h^2}}{J_g} & \frac{b_{33}J_h + b_{32}\sqrt{J_g^2-J_h^2}}{J_g} \\ -\frac{\pi S_x}{2J_g K(\mu)(1-\mu)} & -\frac{\pi S_y}{2J_g K(\mu)} & -\frac{\pi S_z}{2J_g K(\mu)(1-\mu)} \\ \frac{\mathcal{T} S_x}{1-\mu} - \frac{b_{11}J_h}{J_g\sqrt{J_g^2-J_h^2}} & \mathcal{T} S_y - \frac{b_{21}J_h}{J_g\sqrt{J_g^2-J_h^2}} & \frac{\mathcal{T} S_z}{1-\mu} - \frac{b_{31}J_h}{J_g\sqrt{J_g^2-J_h^2}} \\ \frac{b_{11}}{\sqrt{J_g^2-J_h^2}} & \frac{b_{21}}{\sqrt{J_g^2-J_h^2}} & \frac{b_{31}}{\sqrt{J_g^2-J_h^2}} \end{bmatrix}, \tag{16}$$

with

$$\mathcal{T} = \frac{\left(\Pi_1(-\kappa,\mu) - (1-\zeta)K(m)\right)\sqrt{1+\kappa}}{J_g K(\mu)\sqrt{\zeta}}, \tag{17}$$

$$S_x = \frac{\mathrm{dn}(u,\mu)\mathrm{sn}(u,\mu) - \mathrm{cn}(u,\mu)\mathrm{zn}(u,\mu)}{\sqrt{1-\zeta}}, \tag{18}$$

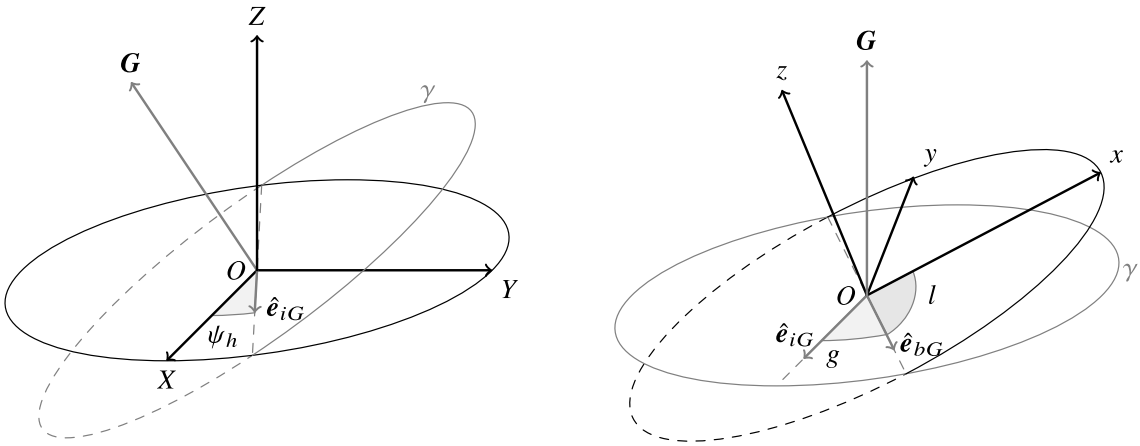

Fig. 1. Significant rotation angles to describe the orientation of the rotating frame $Oxyz$ with respect to the reference frame $OXZY$. In the figure, $\boldsymbol{G}$ is the angular momentum of the satellite.

$$S_y = \frac{\mathrm{dn}(u,\mu)\mathrm{cn}(u,\mu) + \mathrm{sn}(u,\mu)\mathrm{zn}(u,\mu)}{\sqrt{1+\kappa}\sqrt{1-\zeta}}, \tag{19}$$

$$S_z = \frac{\mathrm{dn}(u,\mu)\mathrm{zn}(u,\mu) - \mu\mathrm{cn}(u,\mu)\mathrm{sn}(u,\mu)}{\sqrt{\zeta}}, \tag{20}$$

and $\mathrm{zn}(u,\mu)$ the Jacobi zeta function [see 28].

We recall that the modified Sadov variables are suitable for studying the rotational dynamics of triaxial objects (i.e. $A \neq B \neq C$) or axisymmetric objects with either $A = B$ or $B = C$. In the case of spherical-symmetric bodies with $A = B = C$, one should employ the Andoyer–Serret variables instead. This last case is not treated in the current work.

In this work, the frame $OXYZ$ is obtained by translating the axes of an inertial equatorial geocentric reference frame $EXYZ$ to the satellite's centre of mass.

3. Atmospheric drag models

We consider two alternative models for the atmospheric drag, which differ mainly in two aspects:

1. the dimensionless drag coefficient;
2. the existence of a lift component of the force.

We consider a mid-fidelity model based on Sentman's model [see 25] in which the force has both a drag component and a lift component and the associated dimensionless coefficients depend on the satellite's attitude and several properties of the atmosphere besides the density, namely the temperature and the number density of its chemical species. This model necessarily has to rely on advanced atmospheric models to retrieve these quantities, such as the *nrlmsise00* [see 29]. Using simpler exponential atmospheric models, which do not provide the required data, would make it impossible to compute the lift component of the force and part of the drag component. In this case, one can employ a simplified low-fidelity model of the aerodynamic force, which neglects the lift component and assumes a constant dimensional drag coefficient, as done in [17,21,30].

3.1. Low-fidelity model

The atmospheric drag force acting on a surface element $\mathrm{d}S$ of the satellite is

$$\mathrm{d}\boldsymbol{f}_\mathrm{d} = -\frac{1}{2} c_D \rho_a \tilde{V} \max\left(\hat{\boldsymbol{n}}_s \cdot \frac{\tilde{\boldsymbol{V}}}{\tilde{V}}, 0\right) \tilde{\boldsymbol{V}} \mathrm{d}S, \tag{21}$$

and the corresponding elementary torque is

$$\mathrm{d}\boldsymbol{M}_\mathrm{d} = \boldsymbol{\rho}_s \times \mathrm{d}\boldsymbol{f}_\mathrm{d}, \tag{22}$$

[see 21], where

- c_D is a coefficient, typically assumed equal to 2.2 [see 17],
- ρ_a is the stream density,
- $\hat{\boldsymbol{n}}_s$ is outer-pointing unit normal vector of the surface element,
- $\boldsymbol{\rho}_s$ is the vector from the centre of mass to the surface element,

– $\tilde{\boldsymbol{V}}$ is the velocity of the surface element relative to the incident stream, and $\tilde{V} = |\tilde{\boldsymbol{V}}|$.

In particular,

$$\tilde{\boldsymbol{V}} = \boldsymbol{\omega} \times \boldsymbol{\rho}_s + \boldsymbol{V}_0, \tag{23}$$

with $\boldsymbol{\omega}$ the satellite's angular velocity and

$$\boldsymbol{V}_0 = \mathbf{R}_{\mathrm{i2b}} \left(\dot{\boldsymbol{r}} - n_{\oplus} \hat{\boldsymbol{e}}_Z \times \boldsymbol{r} \right), \tag{24}$$

where $\boldsymbol{r}$ and $\dot{\boldsymbol{r}}$ are the geocentric position vector and the velocity vector of the satellite's centre of mass, respectively, $n_{\oplus} = 4.178074622291 \cdot 10^{-3} \frac{\mathrm{deg}}{\mathrm{s}}$ [see 31], and $\hat{\boldsymbol{e}}_Z$ is the unit vector corresponding to the Z axis. Typically, $|\boldsymbol{\omega} \times \boldsymbol{\rho}_s| < |\boldsymbol{V}_0|$. Thus, we introduce the approximation

$$\tilde{\boldsymbol{V}} \sim \boldsymbol{V}_0. \tag{25}$$

Set

$$V_0 = |\boldsymbol{V}_0|, \quad \hat{\boldsymbol{e}}_0 = \frac{\boldsymbol{V}_0}{V_0}. \tag{26}$$

It follows

$$\boldsymbol{f}_{\mathrm{d}} \sim -\frac{1}{2} c_D \rho_a V_0^2 \int \max\left(\hat{\boldsymbol{n}}_s \cdot \hat{\boldsymbol{e}}_0, 0\right) \hat{\boldsymbol{e}}_0 \mathrm{d}S, \tag{27}$$

and

$$\boldsymbol{M}_{\mathrm{d}} \sim -\frac{1}{2} c_D \rho_a V_0^2 \int \max\left(\hat{\boldsymbol{n}}_s \cdot \hat{\boldsymbol{e}}_0, 0\right) \boldsymbol{\rho}_s \times \hat{\boldsymbol{e}}_0 \mathrm{d}S. \tag{28}$$

We subdivide the satellite surface into n_f facets. Each ith facet has an outer-pointing normal unit vector $\hat{\boldsymbol{n}}_i$ and surface area S_i. Using the approximation

$$\max\left(\hat{\boldsymbol{n}}_i \cdot \hat{\boldsymbol{e}}_0, 0\right) \sim d_i = \frac{1}{3\pi} + \frac{1}{2}(\hat{\boldsymbol{n}}_i \cdot \hat{\boldsymbol{e}}_0) + \frac{4}{3\pi}(\hat{\boldsymbol{n}}_i \cdot \hat{\boldsymbol{e}}_0)^2, \tag{29}$$

it results

$$\boldsymbol{f}_{\mathrm{d}} = -\frac{1}{2} c_D \rho_a V_0^2 \sum_i^{n_f} S_i d_i \hat{\boldsymbol{e}}_0, \tag{30}$$

and

$$\boldsymbol{M}_{\mathrm{d}} = -\frac{1}{2} c_D \rho_a V_0^2 \sum_i^{n_f} S_i d_i \boldsymbol{\rho}_i \times \hat{\boldsymbol{e}}_0, \tag{31}$$

with $\boldsymbol{\rho}_i$ the vector from the centre of mass to the centroid of the ith facet. This model does not account for the facets' self-shadowing effects. Different atmospheric models can be used for the stream density. We use the exponential atmospheric model described by Table 7.4 in [31].

3.2. Mid-fidelity model

As in the low-fidelity model, the satellite's external surface is subdivided into n_f facets and the atmospheric drag force is computed as the sum of the forces acting on each facet, i.e.

$$\boldsymbol{f}_{\mathrm{d}} = \sum_i^{n_f} \boldsymbol{f}_{\mathrm{d},i}, \tag{32}$$

$$\boldsymbol{f}_{\mathrm{d},i} = -\frac{1}{2} \rho_a V_0^2 S_i \left(c_{D,i} \hat{\boldsymbol{e}}_0 + c_{L,i} \hat{\boldsymbol{e}}_0 \times (\hat{\boldsymbol{n}}_i \times \hat{\boldsymbol{e}}_0) \right), \tag{33}$$

with $c_{D,i}$ and $c_{L,i}$ the ith drag and lift coefficients, respectively [see 22]. In Sentman's model [see 24], assuming a unitary accommodation coefficient, $c_{D,i}$ and $c_{L,i}$ are equal to:

$$c_{D,i} = \max(\hat{\boldsymbol{e}}_0 \cdot \hat{\boldsymbol{n}}_i, 0) + c_{d,i} + (\hat{\boldsymbol{e}}_0 \cdot \hat{\boldsymbol{n}}_i) c_{L,i}, \tag{34}$$

$$c_{L,i} = c_{l,i} + \frac{\sqrt{\pi}}{2\mathcal{S}_0} \sqrt{\frac{T_W}{T_0}} (\max(\hat{\boldsymbol{e}}_0 \cdot \hat{\boldsymbol{n}}_i, 0) + c_{d,i}), \tag{35}$$

with

$$c_{d,i} = \frac{\exp\left(-\mathcal{S}_i^2\right)}{\sqrt{\pi}\mathcal{S}_0} \max\left(\frac{\hat{\boldsymbol{e}}_0 \cdot \hat{\boldsymbol{n}}_i}{|\hat{\boldsymbol{e}}_0 \cdot \hat{\boldsymbol{n}}_i|}, 0 \right) + \max(\hat{\boldsymbol{e}}_0 \cdot \hat{\boldsymbol{n}}_i, 0) \mathrm{erf}(\mathcal{S}_i), \tag{36}$$

$$c_{l,i} = \frac{1 + \mathrm{erf}(\mathcal{S}_i)}{2\mathcal{S}_0^2} \max\left(\frac{\hat{\boldsymbol{e}}_0 \cdot \hat{\boldsymbol{n}}_i}{|\hat{\boldsymbol{e}}_0 \cdot \hat{\boldsymbol{n}}_i|}, 0 \right), \tag{37}$$

and

$$\mathcal{S}_i = \mathcal{S}_0(\hat{\boldsymbol{e}}_0 \cdot \hat{\boldsymbol{n}}_i), \tag{38}$$

where erf is the error function [see 27], T_W is the wall temperature, T_0 is the atmospheric temperature, and $\mathcal{S}_0$ is the molecular speed ratio. In particular, given the atmospheric molar mass $\mathcal{M}$, i.e.

$$\mathcal{M} = \frac{\sum_j n_j \mathcal{M}_j}{\sum_j n_j}, \tag{39}$$

with $\mathcal{M}_j$ and n_j the molar mass and the number density of the jth air component, the molecular speed ratio is

$$\mathcal{S}_0 = \frac{V_0}{\sqrt{\frac{2\mathsf{R}T_0}{\mathcal{M}}}}, \tag{40}$$

where $\mathsf{R} = 8.314472\ \frac{\mathrm{J}}{\mathrm{molK}}$ is the ideal gas constant. The wall temperature can be considered constant, to a first approximation, with a value ~300 K [32,33]. Instead, the atmospheric temperature and $\mathcal{S}_0$ change depending on the epoch, the longitude, the latitude, and, mainly, the altitude of the satellite. Typically, T_0 increases with the altitude while $\mathcal{S}_0$ decreases.

The total drag torque is

$$\boldsymbol{M}_{\mathrm{d}} = \sum_i^{n_f} \boldsymbol{\rho}_i \times \boldsymbol{f}_{\mathrm{d},i}. \tag{41}$$

Note that, when $\hat{\boldsymbol{e}}_0 \cdot \hat{\boldsymbol{n}}_i = 0$, the coefficients $c_{d,i}$ and $c_{l,i}$ have jump discontinuities, causing jump discontinuities also in the resultant torque. Discontinuities of this kind are undesirable not only because they make the determination of a suitable averaged attitude model more complex, but also because they affect the numerical integration of the (non-averaged) equations of motion. To avoid this non-continuous situation, similarly to [23], $c_{d,i}$ and $c_{l,i}$ are replaced by their fourth-order Chebyshev expansion:

$$\begin{aligned}
c_{d,i} &\sim \tilde{c}_{d,i} = \mathsf{a}_0 + \mathsf{a}_1(\hat{\boldsymbol{e}}_0 \cdot \hat{\boldsymbol{n}}_i) + \mathsf{a}_2(\hat{\boldsymbol{e}}_0 \cdot \hat{\boldsymbol{n}}_i)^2 + \mathsf{a}_3(\hat{\boldsymbol{e}}_0 \cdot \hat{\boldsymbol{n}}_i)^3 + \mathsf{a}_4(\hat{\boldsymbol{e}}_0 \cdot \hat{\boldsymbol{n}}_i)^4,\\
c_{l,i} &\sim \tilde{c}_{l,i} = \mathsf{b}_0 + \mathsf{b}_1(\hat{\boldsymbol{e}}_0 \cdot \hat{\boldsymbol{n}}_i) + \mathsf{b}_2(\hat{\boldsymbol{e}}_0 \cdot \hat{\boldsymbol{n}}_i)^2 + \mathsf{b}_3(\hat{\boldsymbol{e}}_0 \cdot \hat{\boldsymbol{n}}_i)^3 + \mathsf{b}_4(\hat{\boldsymbol{e}}_0 \cdot \hat{\boldsymbol{n}}_i)^4,
\end{aligned}$$

with

$$\begin{aligned}
\mathsf{a}_0 &= -\frac{\exp\left(-\frac{\mathcal{S}_0^2}{2}\right)}{10\sqrt{\pi}\mathcal{S}_0^3}\left((\mathcal{S}_0^4 + 6\mathcal{S}_0^2 - 8)\tilde{\mathcal{I}}_1\left(\frac{\mathcal{S}_0^2}{2}\right) + \mathcal{S}_0^2(\mathcal{S}_0^2 + 7)\tilde{\mathcal{I}}_0\left(\frac{\mathcal{S}_0^2}{2}\right)\right),\\
\mathsf{a}_1 &= \frac{80}{3\pi^{3/2}\mathcal{S}_0^4}\left(\mathcal{S}_0^5\,\mathrm{pFq}\left(\begin{matrix}1/2, & 2\\ 3/2, & 5/2\end{matrix}, -\mathcal{S}_0^2\right) - \frac{24\mathcal{S}_0^5}{25}\,\mathrm{pFq}\left(\begin{matrix}1/2, & 3\\ 3/2, & 7/2\end{matrix}, -\mathcal{S}_0^2\right)\right.\\
&\quad\left. + \frac{3\sqrt{\pi}(\mathcal{S}_0^2 + 3)\mathrm{i}\,\mathrm{erf}(\mathrm{i}\mathcal{S}_0)\exp(-\mathcal{S}_0^2)}{40} + \frac{9\mathcal{S}_0}{20}\right),\\
\mathsf{a}_2 &= \frac{2\exp\left(-\frac{\mathcal{S}_0^2}{2}\right)}{5\sqrt{\pi}\mathcal{S}_0^3}\left((3\mathcal{S}_0^4 - 4\mathcal{S}_0^2)\tilde{\mathcal{I}}_0\left(\frac{\mathcal{S}_0^2}{2}\right)(3\mathcal{S}_0^4 - 7\mathcal{S}_0^2 + 16)\tilde{\mathcal{I}}_1\left(\frac{\mathcal{S}_0^2}{2}\right)\right),\\
\mathsf{a}_3 &= -\frac{24}{\pi^{3/2}\mathcal{S}_0^4}\left(\mathcal{S}_0^5\,\mathrm{pFq}\left(\begin{matrix}1/2, & 2\\ 3/2, & 5/2\end{matrix}, -\mathcal{S}_0^2\right) - \frac{16\mathcal{S}_0^5}{15}\,\mathrm{pFq}\left(\begin{matrix}1/2, & 3\\ 3/2, & 7/2\end{matrix}, -\mathcal{S}_0^2\right)\right.\\
&\quad\left. + \frac{\sqrt{\pi}(\mathcal{S}_0^2 + 2)\,\mathrm{i}\,\mathrm{erf}(\mathrm{i}\,\mathcal{S}_0)\exp(-\mathcal{S}_0^2)}{8} + \frac{\mathcal{S}_0}{2}\right),\\
\mathsf{a}_4 &= -\frac{8\exp\left(-\frac{\mathcal{S}_0^2}{2}\right)}{15\sqrt{\pi}\mathcal{S}_0^3}\left(\mathcal{S}_0^2(\mathcal{S}_0^2 - 3)\tilde{\mathcal{I}}_0\left(\frac{\mathcal{S}_0^2}{2}\right) + (\mathcal{S}_0^4 - 4\mathcal{S}_0^2 + 12)\tilde{\mathcal{I}}_1\left(\frac{\mathcal{S}_0^2}{2}\right)\right),\\
\mathsf{b}_0 &= \frac{1}{4\mathcal{S}_0^2} - \frac{40}{3\pi^{3/2}\mathcal{S}_0}\,\mathrm{pFq}\left(\begin{matrix}1/2, & 2\\ 3/2, & 5/2\end{matrix}, -\mathcal{S}_0^2\right) + \frac{128}{15\pi^{3/2}\mathcal{S}_0}\,\mathrm{pFq}\left(\begin{matrix}1/2, & 3\\ 3/2, & 7/2\end{matrix}, -\mathcal{S}_0^2\right)\\
&\quad + \frac{5}{\pi^{3/2}\mathcal{S}_0}\,\mathrm{pFq}\left(\begin{matrix}1/2, & 1\\ 3/2, & 3/2\end{matrix}, -\mathcal{S}_0^2\right),\\
\mathsf{b}_1 &= \frac{\exp\left(-\frac{\mathcal{S}_0^2}{2}\right)}{\sqrt{\pi}\mathcal{S}_0^3}\left(\mathcal{S}_0^2\tilde{\mathcal{I}}_0\left(\frac{\mathcal{S}_0^2}{2}\right) + (\mathcal{S}_0^2 - 2)\tilde{\mathcal{I}}_1\left(\frac{\mathcal{S}_0^2}{2}\right)\right) + \frac{2}{\pi\mathcal{S}_0^2},\\
\mathsf{b}_2 &= \frac{4}{\pi^{3/2}\mathcal{S}_0}\left(\frac{68}{3}\,\mathrm{pFq}\left(\begin{matrix}1/2, & 2\\ 3/2, & 5/2\end{matrix}, -\mathcal{S}_0^2\right) - \frac{256}{15}\,\mathrm{pFq}\left(\begin{matrix}1/2, & 3\\ 3/2, & 7/2\end{matrix}, -\mathcal{S}_0^2\right)\right.
\end{aligned}$$

$$- 5\,\mathrm{pFq}\left(\begin{matrix} 1/2, & 1 \\ 3/2, & 3/2 \end{matrix}, -\mathcal{S}_0^2\right)\Bigg),$$

$$\mathtt{b}_3 = -\frac{\exp\left(-\frac{\mathcal{S}_0^2}{2}\right)}{2\sqrt{\pi}\mathcal{S}_0^3}\left(\mathcal{S}_0^2\tilde{\mathcal{I}}_0\left(\frac{\mathcal{S}_0^2}{2}\right) + (\mathcal{S}_0^2 - 4)\tilde{\mathcal{I}}_1\left(\frac{\mathcal{S}_0^2}{2}\right)\right) - \frac{1}{\pi\mathcal{S}_0^2},$$

$$\mathtt{b}_4 = -\frac{16}{\pi^{3/2}\mathcal{S}_0}\left(\frac{16}{3}\,\mathrm{pFq}\left(\begin{matrix} 1/2, & 2 \\ 3/2, & 5/2 \end{matrix}, -\mathcal{S}_0^2\right) - \frac{64}{15}\,\mathrm{pFq}\left(\begin{matrix} 1/2, & 3 \\ 3/2, & 7/2 \end{matrix}, -\mathcal{S}_0^2\right)\right.$$

$$\left. - \mathrm{pFq}\left(\begin{matrix} 1/2, & 1 \\ 3/2, & 3/2 \end{matrix}, -\mathcal{S}_0^2\right)\right),$$

where $\mathtt{i}$ is the imaginary unit, $\tilde{\mathcal{I}}_\mathtt{k}(\mathtt{x})$ are the modified Bessel functions of first kind [see27, Chapter 10], and $\mathrm{pFq}\left(\begin{matrix} \mathtt{a}_1, & \cdots, \mathtt{a}_N \\ \mathtt{b}_1, & \cdots, \mathtt{b}_N \end{matrix}, \mathtt{x}\right)$ is the generalised hypergeometrix function [see27, Chapter 16]. We also introduce the same approximation in Eq. (29). Thus,

$$\boldsymbol{f}_\mathrm{d} \sim \sum_i^{n_f} \tilde{\boldsymbol{f}}_{\mathrm{d},i}, \tag{42}$$

and

$$\boldsymbol{M}_\mathrm{d} \sim \sum_i^{n_f} \boldsymbol{\rho}_i \times \tilde{\boldsymbol{f}}_{\mathrm{d},i}. \tag{43}$$

where

$$\tilde{\boldsymbol{f}}_{\mathrm{d},i} = -\frac{1}{2}\rho_a V_0^2 S_i\left(\left(d_i + \tilde{c}_{d,i}\right)\hat{\boldsymbol{e}}_0 + \left(\tilde{c}_{l,i} + \frac{\sqrt{\pi}}{2\mathcal{S}_0}\sqrt{\frac{T_W}{T_0}}(d_i + \tilde{c}_{d,i})\right)\hat{\boldsymbol{n}}_i\right). \tag{44}$$

This model does not account for the facets' self-shadowing effects. The *nrlmsise00* atmospheric model is used to compute the atmospheric density, the atmospheric temperature and the number densities of the air components, namely helium (He), atomic oxygen (O), molecular oxygen (O_2), atomic nitrogen (N), molecular nitrogen (N_2), argon (Ar) and atomic hydrogen (H).

4. Averaged model

The averaged model is determined following the same logic and the same steps described in detail in [1].

If the artificial satellite were not affected by any perturbation the only non-constant attitude variables are the angles ψ_l and ψ_g and the only non-constant orbital element is the orbital mean anomaly M. Under the hypothesis that the effects of external torques are just perturbations of the free-torque problem, all the other attitude variables in $\boldsymbol{s}$ are expected to have a slower evolution in comparison to ψ_l, ψ_g and M, which, thus, are considered as the fast variables of the problem [see 5,34]. Under the hypothesis that the fast angles of the problem are not resonant and assuming that the satellite is fast-rotating along a Keplerian orbit, we perform a transformation from the osculating $\boldsymbol{s}$ to mean variables $\bar{\boldsymbol{s}}$ such that the vector field

$$\frac{\mathrm{d}\boldsymbol{s}(t)}{\mathrm{d}t} = \mathbf{A}\nabla_{\boldsymbol{s}}\boldsymbol{\Phi} + \mathbf{B}\boldsymbol{M}_\mathrm{d} \tag{45}$$

is transformed into

$$\frac{\mathrm{d}\bar{\boldsymbol{s}}(t)}{\mathrm{d}t} = \mathbf{A}\nabla_{\boldsymbol{s}}\boldsymbol{\Phi} + \frac{1}{8\pi^3}\int_0^{2\pi}\int_0^{2\pi}\int_0^{2\pi}\mathbf{B}\boldsymbol{M}_\mathrm{d}\mathrm{d}\psi_g\mathrm{d}\psi_l\mathrm{d}M + \boldsymbol{R}, \tag{46}$$

where the remainder $\boldsymbol{R}$ is supposed to have a small magnitude, and thus, can be neglected:

$$\frac{\mathrm{d}\bar{\boldsymbol{s}}(t)}{\mathrm{d}t} \sim \mathbf{A}\nabla_{\boldsymbol{s}}\boldsymbol{\Phi} + \frac{1}{8\pi^3}\int_0^{2\pi}\int_0^{2\pi}\int_0^{2\pi}\mathbf{B}\boldsymbol{M}_\mathrm{d}\mathrm{d}\psi_g\mathrm{d}\psi_l\mathrm{d}M. \tag{47}$$

Computing the integral in (47) allows us to derive the first-order averaged model. Several techniques may be used to estimate the transformation from osculating to mean variables $\boldsymbol{s} \to \bar{\boldsymbol{s}}$. For example, one could exploit a numerical method similarly as in [35].

In line with our previous work [1], the transformation is here estimated using the Lie series approach, which will be discussed in the next section.

Here, we describe the semi-analytical procedure used to compute the integral in (47).

Not to oversimplify the atmospheric drag model, we decide to compute the average over (ψ_l, ψ_g) analytically and the average over M numerically. To describe the orbital dynamics of the satellite, the equinoctial elements $\boldsymbol{o} = (a, P_1, P_2, Q_1, Q_2, \Lambda)$ are used, where a is the semi-major axis,

$$P_1 = e\sin(\omega + \Omega),$$
$$P_2 = e\cos(\omega + \Omega),$$
$$Q_1 = \tan\left(\frac{I}{2}\right)\sin\Omega,$$
$$Q_2 = \tan\left(\frac{I}{2}\right)\cos\Omega,$$

with e, I, ω, and Ω the orbital eccentricity, inclination, argument of the perigee, and longitude of the node, respectively, and Λ is the true longitude [see 36]. Let us remark that the dynamics depends on M through Λ.

Each component of the atmospheric drag torque due to the interaction with the ith facet can be expressed as

$$M_{\mathrm{d}_{i,\ell}} = \delta_{c_D} \sum_{p,q,w} C_p(J_h, \psi_h; S_i, \hat{\boldsymbol{n}}_i, \boldsymbol{\rho}_i)\, \mathcal{F}_q(\boldsymbol{o})\, \mathcal{B}_w, \tag{48}$$

where $\mathcal{B}_w$ is some combination of the elements b_{jk} in (4)–(12), and either $\delta c_D = c_D$ if $\boldsymbol{M}_{\mathrm{d}}$ is given by (31) or $\delta_{c_D} = 1$ if $\boldsymbol{M}_{\mathrm{d}}$ is given by (43). Since $\mathbf{B}$ does not depend on the orbital elements, the $\mathcal{F}_q$ terms are the only terms in the vector field $\mathbf{B}\boldsymbol{M}_{\mathrm{d}}$ depending on the orbital mean anomaly through the true longitude. Thus, it is possible to isolate them and numerically compute their average over M, i.e.

$$\frac{1}{2\pi}\int_0^{2\pi} \frac{\left(1 - P_1^2 - P_2^2\right)^{\frac{3}{2}} \mathcal{F}_q(\boldsymbol{o})}{\left(1 + P_1 \sin\Lambda + P_2 \cos\Lambda\right)^2} \mathrm{d}\Lambda, \tag{49}$$

using for example the trapezoidal rule or the Gaussian quadrature rule. Instead, the dependence on (ψ_l, ψ_g) occurs through the $\mathcal{B}_w$ terms for the torques, and the b_{jk} elements, S_x, S_y and S_z for the matrix $\mathbf{B}$. Thus, it is necessary to compute

$$\frac{1}{4\pi^2}\int_0^{2\pi}\int_0^{2\pi} \mathcal{B}_w b_{jk} \mathrm{d}\psi_g \mathrm{d}\psi_l \tag{50}$$

and

$$\frac{1}{4\pi^2}\int_0^{2\pi}\int_0^{2\pi} \mathcal{B}_w S_\xi \mathrm{d}\psi_g \mathrm{d}\psi_l, \quad \xi = x, y, z. \tag{51}$$

This can be easily done analytically with the support of a symbolic manipulator such as MAPLE, performing first the integration over ψ_g and then the integration over ψ_l, as described in [1].

Let us remark that the resulting averaged model is suitable only in the hypothesis that the effects of atmospheric drag are perturbations of the torque-free problem. Thus, if the satellite is not a fast rotator or it is at very low altitudes, where the impact of the atmospheric drag is significant [see 21], the averaged model may be inaccurate. We suggest the application of our averaged solution to fast-rotating satellites at altitudes above 800 km. Another limit is related to the rotational state vector of the satellite. We recall that the condition $J_d = B$ (see Eq. (1)) identifies the separatrix between the SAMs and the LAMs in the torque-free problem [see 13]. When this problem is perturbed the region of the phase space surrounding the separatrix becomes chaotic. When the rotational state falls inside the chaotic region of the phase space or is very close to it, the averaged model becomes unsuitable [see 37]. For triaxial satellites, conditions $J_d = B$ correspond to $\mu = 1$, thus this quantity can be used to check the proximity to the chaotic region [see 1].

The averaged equations of motion and transformations are available open source at this link:
https://github.com/strath-ace/smart-astro/tree/opensource_release/JULIA.

Once the transformation from osculating to mean variables is performed, it is possible to integrate the averaged equations of motion by using the mean variables as initial conditions.

5. Osculating to mean variables transformation

The transformation from osculating to mean variables is determined using the Lie series approach. We recall that a Lie transformation is a transformation between two sets of variables $\boldsymbol{s}^{(0)}$ and $\boldsymbol{s}^{(1)}$ given by

$$\boldsymbol{s}^{(0)} = \sum_{i=0}^{\infty} \frac{1}{i!} \mathcal{L}_{\boldsymbol{W}}^i \boldsymbol{s}^{(1)}, \tag{52}$$

with

$$\mathcal{L}_{\boldsymbol{W}}^i(\boldsymbol{s}^{(1)}) = \underbrace{\mathcal{L}_{\boldsymbol{W}}\left(\mathcal{L}_{\boldsymbol{W}}\left(\ldots\left(\mathcal{L}_{\boldsymbol{W}}\boldsymbol{s}^{(1)}\right)\right)\right)}_{i \text{ times}}, \tag{53}$$

where $\mathcal{L}_{\boldsymbol{W}}\boldsymbol{s}^{(1)}$ is the Lie derivative of $\boldsymbol{s}^{(1)}$ with respect to the generator $\boldsymbol{W}$ [see 20]. A vector field $\boldsymbol{F}$ depending on $\boldsymbol{s}^{(0)}$ is transformed into

$$\boldsymbol{F}'(\boldsymbol{s}^{(1)}) = \sum_{i=0}^{\infty} \frac{1}{i!} \tilde{\mathcal{L}}_{\boldsymbol{W}}^i \boldsymbol{F}(\boldsymbol{s}^{(0)})\big|_{\boldsymbol{s}^{(0)}=\boldsymbol{s}^{(1)}}, \tag{54}$$

with

$$\tilde{\mathcal{L}}_{\boldsymbol{W}}^i \boldsymbol{F}(\boldsymbol{s}^{(0)}) = \underbrace{\tilde{\mathcal{L}}_{\boldsymbol{W}}\left(\tilde{\mathcal{L}}_{\boldsymbol{W}}\left(\ldots\left(\tilde{\mathcal{L}}_{\boldsymbol{W}}\boldsymbol{F}\left(\boldsymbol{s}^{(0)}\right)\right)\right)\right)}_{i \text{ times}}, \tag{55}$$

where

$$\tilde{\mathcal{L}}_{\boldsymbol{W}} \cdot = \frac{\partial \cdot}{\partial \boldsymbol{s}^{(0)}} \boldsymbol{W} - \frac{\partial \boldsymbol{W}}{\partial \boldsymbol{s}^{(0)}} \cdot \tag{56}$$

is the Lie operator [see 38]. In the following, we drop the subscripts used to distinguish the variables before and after the Lie transformation to simplify the notation. Before applying the Lie series approach, the set of variables $\boldsymbol{s}$ is extended to

$$\tilde{\mathbf{s}} = \left(\zeta, J_g, J_h, \psi_l, \psi_g, \psi_h, J_M, M\right), \tag{57}$$

with J_M a dummy action conjugated to the mean anomaly M, so that the system of equations of motion becomes autonomous. Furthermore, we also introduce the *book-keeping parameter* ε [see 39], which is a formal parameter whose numerical value is equal to one and whose powers are used to keep track of the different relative sizes of the terms characterising the vector field. In the hypothesis of a fast-rotating satellite:

$$\frac{\mathrm{d}\tilde{\mathbf{s}}}{\mathrm{d}t} = \tilde{\mathbf{A}}\nabla_{\tilde{\mathbf{s}}}\boldsymbol{\Phi} + \varepsilon\tilde{\mathbf{A}}\nabla_{\tilde{\mathbf{s}}}\left(nJ_M\right) + \varepsilon^2\tilde{\mathbf{B}}\boldsymbol{M}_{\mathrm{d}}, \tag{58}$$

with n the orbital mean motion and

$$\tilde{\mathbf{A}} = \begin{bmatrix} \mathbf{A} & 0 \\ 0 & \mathbf{J} \end{bmatrix}, \quad \tilde{\mathbf{B}} = \begin{bmatrix} \mathbf{B} & 0 \\ 0 & 0 \end{bmatrix}, \quad \mathbf{J} = \begin{bmatrix} 0 & -1 \\ 1 & 0 \end{bmatrix}. \tag{59}$$

Three successive Lie transformations can be performed:

1. The first transformation has generator $\boldsymbol{W}_1$, fulfilling

$$\tilde{\mathscr{L}}_{\boldsymbol{W}_1}\tilde{\mathbf{A}}\nabla_{\tilde{\mathbf{s}}}\boldsymbol{\Phi} + \varepsilon^2\tilde{\mathbf{B}}\boldsymbol{M}_{\mathrm{d}} = \varepsilon^2\boldsymbol{Z}_2, \quad \boldsymbol{Z}_2 = \frac{1}{4\pi^2}\int_0^{2\pi}\int_0^{2\pi}\tilde{\mathbf{B}}\boldsymbol{M}_{\mathrm{d}}\mathrm{d}\psi_g\mathrm{d}\psi_l, \tag{60}$$

and

$$\frac{1}{2\pi}\int_0^{2\pi}\int_0^{2\pi}\boldsymbol{W}_1\mathrm{d}\psi_g\mathrm{d}\psi_l = \mathbf{0}, \tag{61}$$

and transforms the vector field into

$$\frac{\mathrm{d}\tilde{\mathbf{s}}^{(1)}}{\mathrm{d}t} = \tilde{\mathbf{A}}\nabla_{\tilde{\mathbf{s}}}\boldsymbol{\Phi} + \varepsilon\tilde{\mathbf{A}}\nabla_{\tilde{\mathbf{s}}}\left(nJ_M\right) + \varepsilon^2\boldsymbol{Z}_2 + \mathcal{O}(\varepsilon^3). \tag{62}$$

2. Let $Z_{2,i}$, $i = 1..8$, be the components of $\boldsymbol{Z}_2$, and let $\bar{Z}_{2,i}$ be their average over M. The second transformation has generator

$$\boldsymbol{W}_2 = \frac{2\varepsilon^2}{n_{\psi_g}^2}\begin{bmatrix} n_{\psi_g}\Delta Z_{2,1}\arctan\left(\tan\frac{\psi_g}{2}\right), \\ n_{\psi_g}\Delta Z_{2,2}\arctan\left(\tan\frac{\psi_g}{2}\right) \\ 0 \\ \left(\frac{\partial n_{\psi_l}}{\partial\zeta}\Delta Z_{2,1} + \frac{\partial n_{\psi_l}}{\partial J_g}\Delta Z_{2,2}\right)\left(\arctan^2\left(\tan\frac{\psi_g}{2}\right) - \frac{\pi^2}{12}\right) \\ \left(\frac{\partial n_{\psi_g}}{\partial\zeta}\Delta Z_{2,1} + \frac{\partial n_{\psi_g}}{\partial J_g}\Delta Z_{2,2}\right)\left(\arctan^2\left(\tan\frac{\psi_g}{2}\right) - \frac{\pi^2}{12}\right) \\ 0 \\ 0 \\ 0 \end{bmatrix} \tag{63}$$

with $\Delta Z_{2,1} = Z_{2,1} - \bar{Z}_{2,1}$ and $\Delta Z_{2,2} = Z_{2,2} - \bar{Z}_{2,2}$, and where

$$n_{\psi_l} = -\pi\sqrt{\frac{\zeta}{1+\kappa}}\frac{J_g}{2AC}\frac{C-A}{K(\mu)} \tag{64}$$

and

$$n_{\psi_g} = \left(\Pi(-\kappa,\mu) + \frac{A}{C-A}K(\mu)\right)\frac{J_g(C-A)}{A\,C\,K(\mu)} \tag{65}$$

are the angular speeds of ψ_l and ψ_g, respectively, in the torque-free problem. Note that average of $\boldsymbol{W}_2$ with respect to (ψ_l, ψ_g) is null. The transformed vector field is

$$\frac{\mathrm{d}\tilde{\mathbf{s}}^{(2)}}{\mathrm{d}t} = \tilde{\mathbf{A}}\nabla_{\tilde{\mathbf{s}}}\boldsymbol{\Phi} + \varepsilon\tilde{\mathbf{A}}\nabla_{\tilde{\mathbf{s}}}\left(nJ_M\right) + \varepsilon^2\tilde{\boldsymbol{Z}}_2 + \mathcal{O}(\varepsilon^3), \tag{66}$$

where $\tilde{\boldsymbol{Z}}_2 = \left(\bar{Z}_{2,1}, \bar{Z}_{2,2}, Z_{2,3}, Z_{2,4}, Z_{2,5}, Z_{2,6}, Z_{2,7}, Z_{2,8}\right)^{\mathrm{T}}$.

3. The last transformation has generator $\boldsymbol{W}_3$, fulfilling

$$\tilde{\mathscr{L}}_{\boldsymbol{W}_3}\tilde{\mathbf{A}}\nabla_{\tilde{\mathbf{s}}}(nJ_M) + \varepsilon^2\tilde{\boldsymbol{Z}}_2 = \varepsilon^2\bar{\boldsymbol{Z}}_2, \tag{67}$$

and

$$\frac{1}{2\pi}\int_0^{2\pi}\boldsymbol{W}_3\mathrm{d}M = \mathbf{0}, \tag{68}$$

where $\bar{\boldsymbol{Z}}_2$ is a vector of components $\bar{Z}_{2,i}$, $i = 1..8$. The vector field is transformed into

$$\frac{\mathrm{d}\tilde{\mathbf{s}}^{(3)}}{\mathrm{d}t} = \tilde{\mathbf{A}}\nabla_{\tilde{\mathbf{s}}}\boldsymbol{\Phi} + \varepsilon^2\bar{\boldsymbol{Z}}_2 + \mathcal{O}(\varepsilon^3). \tag{69}$$

Applying (52), and combining the transformations, we obtain that the mean variables can be computed as

$$\bar{\tilde{s}} = \tilde{s} - \boldsymbol{W}_1(\tilde{s}) - \boldsymbol{W}_2\left(\tilde{s} - \boldsymbol{W}_1(\tilde{s})\right) - \boldsymbol{W}_3\left(\tilde{s} - \boldsymbol{W}_1(\tilde{s}) - \boldsymbol{W}_2\left(\tilde{s} - \boldsymbol{W}_1(\tilde{s})\right)\right). \tag{70}$$

5.1. Computation of the generator $\boldsymbol{W}_1$

When the parameter κ differs from zero, the dependence of $\tilde{\mathbf{B}}\boldsymbol{M}_{\mathrm{d}}$ on ψ_l and ψ_g occurs through Jacobi elliptic functions. Thus, solving (60) analytically is extremely complex. To obtain an approximated analytical solution, it is possible to perform Fourier expansions of the Jacobi elliptic functions to deal with trigonometric functions. In this way, the analytical solution of (60) becomes straightforward and it also fulfils condition (61). Such an approach is not necessary when $\kappa = 0$, as the Jacobi elliptic functions become trigonometric functions so that no expansion is required. The expansion in the Fourier series can be computed following [3]. This analytical approximation is employed for the low-fidelity atmospheric drag model in (31). Instead, if the mid-fidelity model in (43) is used, only part of $\boldsymbol{W}_1$ is analytically estimated following the described approach. In this case, the drag torque model is based on a fourth-order Chebyshev expansion of the drag coefficients (see Section 3.2). The additional Fourier expansions would make the terms to handle too numerous. Thus, we split the problem. We express the aerodynamic torque as the sum of two vectors:

$$\boldsymbol{M}_{\mathrm{d}} = \boldsymbol{M}_{\mathrm{d0-2}} + \boldsymbol{M}_{\mathrm{d3-4}}; \tag{71}$$

one vector, $\boldsymbol{M}_{\mathrm{d0-2}}$, contains only the terms up to the second order of the Chebyshev expansion; the other vector, $\boldsymbol{M}_{\mathrm{d3-4}}$, contains the remaining terms. Then, we apply the previously described approach to analytically solve (60) considering $\boldsymbol{M}_{\mathrm{d0-2}}$ in place of $\boldsymbol{M}_{\mathrm{d}}$. Finally, we numerically estimate an approximation of the generator $\tilde{\boldsymbol{W}}_1$ fulfilling

$$\tilde{\mathscr{L}}_{\tilde{\boldsymbol{W}}_1}\tilde{\mathbf{A}}\nabla_{\tilde{s}}\boldsymbol{\Phi} + \varepsilon^2\tilde{\mathbf{B}}\boldsymbol{M}_{\mathrm{d3-4}} = \frac{\varepsilon^2}{4\pi^2}\int_0^{2\pi}\int_0^{2\pi}\tilde{\mathbf{B}}\boldsymbol{M}_{\mathrm{d3-4}}\mathrm{d}\psi_g\mathrm{d}\psi_l, \tag{72}$$

and

$$\frac{1}{4\pi^2}\int_0^{2\pi}\int_0^{2\pi}\tilde{\boldsymbol{W}}_1\mathrm{d}\psi_l\mathrm{d}\psi_g = \mathbf{0}, \tag{73}$$

and we add it to $\boldsymbol{W}_1$. To understand how the approximation of $\tilde{\boldsymbol{W}}_1$ is computed, consider the ith equation of system (72):

$$n_{\psi_l}\frac{\mathrm{d}\tilde{W}_{1_i}}{\mathrm{d}\psi_l} + n_{\psi_g}\frac{\mathrm{d}\tilde{W}_{1_i}}{\mathrm{d}\psi_g} = \hat{m}_i, \quad \hat{m}_i = m_i - \bar{m}_i \tag{74}$$

where n_{ψ_l} and n_{ψ_g} are defined in (65) and (64), respectively, m_i is the ith component of $\tilde{\mathbf{B}}\boldsymbol{M}_{\mathrm{d3-4}}$, $\bar{m}_i$ is its average over (ψ_l, ψ_g) and $\tilde{W}_{1_i}$ is the corresponding component of $\tilde{\boldsymbol{W}}_1$, which has also to fulfil

$$\int_0^{2\pi}\int_0^{2\pi}\tilde{W}_{1_i}\mathrm{d}\psi_g\mathrm{d}\psi_l = 0. \tag{75}$$

To solve (74) it is possible to employ the method of characteristics. A normal vector to the 2-dimensional surface $\tilde{W}_{1_i}(\psi_l, \psi_g)$ is

$$\frac{1}{4\pi^2}\left(\frac{\mathrm{d}\tilde{W}_{1_i}}{\mathrm{d}\psi_l}, \frac{\mathrm{d}\tilde{W}_{1_i}}{\mathrm{d}\psi_g}, -1\right). \tag{76}$$

Thus, (74) implies that the vector field $(n_{\psi_l}, n_{\psi_g}, \hat{m}_i)$ is tangent to $\tilde{W}_{1_i}(\psi_l, \psi_g)$ at every point. The graph of the solution is the union of integral curves of this vector field. These curves, called characteristics curves, are solutions of the system

$$\begin{cases} \frac{\mathrm{d}\psi_l}{\mathrm{d}t} = n_{\psi_l}, \\ \frac{\mathrm{d}\psi_g}{\mathrm{d}t} = n_{\psi_g}, \\ \frac{\mathrm{d}\tilde{W}_{1_i}}{\mathrm{d}t} = \hat{m}_i(\psi_l, \psi_g). \end{cases} \tag{77}$$

From the first two equations of system (77), we obtain that

$$\psi_g = \tilde{\psi} + \frac{n_{\psi_g}}{n_{\psi_l}}\psi_l, \tag{78}$$

where $\tilde{\psi}$ is the constant of integration, and from the first and last equations, after substituting ψ_g, we get

$$\mathrm{d}\tilde{W}_{1_i} = \frac{\hat{m}_i(\psi_l, \tilde{\psi})}{n_{\psi_l}}\mathrm{d}\psi_l. \tag{79}$$

Thus, the solution of (74) fulfilling condition (75) is

$$\tilde{W}_{1_i}(\psi_l, \tilde{\psi}) = \frac{1}{n_{\psi_l}}\left(G_1(\psi_l, \tilde{\psi}) - \frac{1}{4\pi^2}\int_0^{2\pi}\int_{-\frac{n_{\psi_g}}{n_{\psi_l}}\psi_l}^{2\pi-\frac{n_{\psi_g}}{n_{\psi_l}}\psi_l} G_1(\psi_l, \tilde{\psi})\mathrm{d}\tilde{\psi}\mathrm{d}\psi_l\right), \tag{80}$$

with $G_1(\psi_l, \tilde{\psi})$ the primitive function

$$G_1(\psi_l, \tilde{\psi}) = \int \hat{m}_i(\psi_l, \psi_g)\mathrm{d}\psi_l. \tag{81}$$

The issue in the computation of $\tilde{W}_{1_i}(\psi_l,\tilde{\psi})$ is given by the impossibility of determining $G_1(\psi_l,\tilde{\psi})$ analytically. With some numerical methods, we are able to estimate

$$\mathcal{G}_1(\psi_l,\tilde{\psi}) = G_1(\psi_l,\tilde{\psi}) - G_1(0,\tilde{\psi}). \tag{82}$$

We approximate $\tilde{W}_{1_i}(\psi_l,\tilde{\psi})$ in (80) as

$$\tilde{W}_{1_i}(\psi_l,\tilde{\psi}) \sim \frac{\hat{\mathcal{G}}_1(\psi_l,\tilde{\psi})}{n_{\psi_l}} - \frac{1}{4\pi^2 n_{\psi_l}} \int_0^{2\pi} \int_{-\frac{n_{\psi_g}}{n_{\psi_l}}\psi_l}^{2\pi-\frac{n_{\psi_g}}{n_{\psi_l}}\psi_l} \hat{\mathcal{G}}_1(\psi_l,\tilde{\psi})\mathrm{d}\tilde{\psi}\mathrm{d}\psi_l, \tag{83}$$

with

$$\hat{\mathcal{G}}_1(\psi_l,\tilde{\psi}) = \mathcal{G}_1(\psi_l,\tilde{\psi}) - \frac{1}{2\pi}\int_0^{2\pi} \mathcal{G}_1(\psi_l,\tilde{\psi})\mathrm{d}\psi_l. \tag{84}$$

After some algebra, it results that the difference between the approximated $\tilde{W}_{1_i}(\psi_l,\tilde{\psi})$ in (83) and the correct $\tilde{W}_{1_i}(\psi_l,\tilde{\psi})$ in (80) is the constant term

$$\frac{1}{8\pi^3}\int_0^{2\pi} \int_{-\frac{n_{\psi_g}}{n_{\psi_l}}\psi_l}^{2\pi-\frac{n_{\psi_g}}{n_{\psi_l}}\psi_l} \hat{G}_1(\tilde{\psi})\mathrm{d}\tilde{\psi}\mathrm{d}\psi_l, \tag{85}$$

with

$$\hat{G}_1(\tilde{\psi}) = \frac{1}{2\pi}\int_0^{2\pi} G_1(\psi_l,\tilde{\psi})\mathrm{d}\psi_l. \tag{86}$$

Thus, the approximated $\tilde{W}_{1_i}(\psi_l,\tilde{\psi})$ is still solution of the first equation in (74), but does not exactly fulfil (75), which implies that its average over (ψ_l,ψ_g) will be slightly different from zero.

Let us remark that we could have used the second technique described to numerically estimate an approximation of the overall generator $\boldsymbol{W}_1$. However, in this procedure, all the required integrals have to be numerically estimated so the method is not particularly convenient either in terms of computational time or accuracy. For this reason, it is applied only to handle part of the vector field.

5.2. Computation of the generator $\boldsymbol{W}_3$

Since the average over the mean anomaly is computed numerically, also $\boldsymbol{W}_3$ has to be numerically determined. Let us call W_{3_i}, $\tilde{Z}_{2,i}$ and $\bar{Z}_{2,i}$, $i>2$, the ith components of $\boldsymbol{W}_3$, $\tilde{\boldsymbol{Z}}_2$ and $\bar{\boldsymbol{Z}}_2$. W_{3_i} must fulfil

$$\frac{\mathrm{d}W_{3_i}}{\mathrm{d}\Lambda} = \frac{1}{n}\frac{\eta^3}{\Phi^2}(\tilde{Z}_{2,i} - \bar{Z}_{2,i}) \tag{87}$$

$$\frac{1}{2\pi}\int_0^{2\pi} \frac{\eta^3}{\Phi^2} W_{3_i}\mathrm{d}\Lambda = 0, \tag{88}$$

with $\eta = \sqrt{1-P_1^2-P_2^2}$ and

$$\Phi = 1 + P_1\sin\Lambda + P_2\cos\Lambda. \tag{89}$$

The solution is

$$W_{3_i} = \frac{1}{n}\left(G_3 - \frac{1}{2\pi}\int_0^{2\pi}\frac{\eta^3}{\Phi^2}G_3\mathrm{d}\Lambda\right), \tag{90}$$

with G_3 the primitive

$$G_3 = \int \frac{\eta^3}{\Phi^2}(\tilde{Z}_{2,i} - \bar{Z}_{2,i})\mathrm{d}\Lambda. \tag{91}$$

Also in this case the issue is the analytical computation of G_3. Numerically, it is possible to estimate

$$\mathcal{G}_3(\Lambda) = G_3(\Lambda) - G_3(0). \tag{92}$$

So, we approximate W_{3_i} as

$$W_{3_i} \sim \mathcal{G}_3(\Lambda) - \frac{1}{2\pi}\int_0^{2\pi}\mathcal{G}_3(\Lambda)\mathrm{d}\Lambda. \tag{93}$$

The difference between the correct W_{3_i} in (90) and the approximated W_{3_i} in (93) is

$$\frac{1}{2\pi}\left(\int_0^{2\pi}\frac{\eta^3}{\Phi^2}G_3(\Lambda)\mathrm{d}\Lambda - \int_0^{2\pi}G_3(\Lambda)\mathrm{d}\Lambda\right) \tag{94}$$

which is zero only in the case of a circular orbit. Thus, the approximated solution fulfils (87) but does not exactly fulfil (88). Anyway, it is acceptable for non-highly eccentric orbits.

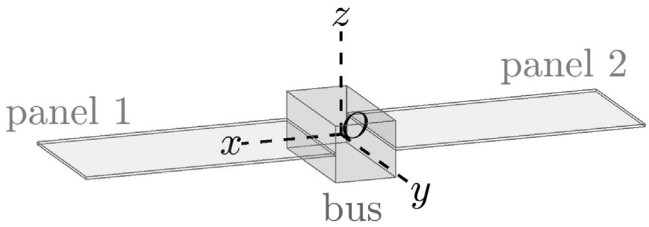

Fig. 2. Triaxial satellite.

Table 1
Characteristics of the triaxial satellite in Fig. 2.

Mass	$m = 500$ kg
Moments of inertia	$A = 334.042$ kg m^2, $B = 2404.958$ kg m^2 $C = 2678.416$ kg m^2
Intrinsic magnetic moment	$\boldsymbol{I}_{\mathrm{m}} = [0.1, 0.1, 0.1]$Am^2
Total reflectivity	bus: 0.6 panels (front): 0.27 panels (back): 0.07
Fraction of the total reflectivity that is specular	bus: 1 panels (front): 1 panels (back): 0

6. Coupling attitude and orbital dynamics

To account for the effects of the orbital variations, the semi-analytical propagation of the attitude is coupled with the analytical integration of the first-order averaged model of the orbital dynamics developed by Zuiani and Vasile [36], Di Carlo et al. [40], Di Carlo et al. [35]. This latter is partially modified to include a model for the perturbative atmospheric drag acceleration in line with the torque considered in the attitude averaged equations of motion. We replace their acceleration model [equations 21–24 in 40] with

$$\boldsymbol{a}_{\mathrm{d}} = \frac{1}{m}\mathbf{R}_{\mathrm{i2o}}\mathbf{R}_{\mathrm{i2b}}^{\mathrm{T}}\boldsymbol{f}_{\mathrm{d}}, \tag{95}$$

with $\boldsymbol{f}_{\mathrm{d}}$ either in (30) or (42), and we compute the average of the Gaussian non-singular planetary equations [see equation 3 in35] over (ψ_l, ψ_g, M), using the same approach described in Section 4.

7. Simulations

In this section we present the result of some numerical experiments. We first compare the value of the mean Sadov variables $\bar{\mathbf{s}}_{SA} = [\bar{\zeta}_{SA}, \bar{J}_{gSA}, \bar{J}_{hSA}, \bar{\psi}_{hSA}]^T$, coming from integrating the averaged model, against the averaged evolution of the non-averaged attitude dynamics, or $\bar{\mathbf{s}}_O = [\bar{\zeta}_O, \bar{J}_{gO}, \bar{J}_{hO}, \bar{\psi}_{hO}]^T$. The non-averaged attitude dynamics is expressed and propagated in quaternions and angular velocity vector [see 41,42] and then converted in $\boldsymbol{s}$ variables before computing the numerical average. Once the body-fixed rotating reference frame $Oxyz$ is defined, as discussed in Section 2, together with the satellite's angular velocity $\boldsymbol{w}$ and quaternions, the transformation to the $\boldsymbol{s}$ variables can be performed passing through the Andoyer–Serret variables. Given the angular velocity and orientation of the satellite, computing the value of the corresponding Andoyer–Serret variables is straightforward as these variables have a clear physical meaning, see [37,43,44]. Then, the transformation to $\boldsymbol{s}$ variables can be obtained by applying the formulas in either [1, Section 2.2] or [5, Sections 2.1-2.2]. Thus, from the evolution of $\boldsymbol{w}$ and the quaternions, one can compute the evolution of the corresponding $\boldsymbol{s}$ variables. Then, the evolution of the mean slow variables can be obtained by performing a double average of the $\boldsymbol{s}$ variables over the time intervals T_{a} and T_{o}, defined as:

$$T_{\mathrm{a}} = \max\left(\frac{2\pi}{n_{\psi_l}}, \frac{2\pi}{n_{\psi_g}}\right), \quad T_{\mathrm{o}} = \frac{2\pi}{n}.$$

Finally the relative difference between $\bar{\mathbf{s}}_{SA}$ and $\bar{\mathbf{s}}_O$ is defined as:

$$\Delta\zeta = 100\left|\frac{\bar{\zeta}_{\mathrm{O}} - \bar{\zeta}_{\mathrm{SA}}}{\bar{\zeta}_{\mathrm{O}}}\right|, \tag{96}$$

$$\Delta J_g = 100\left|\frac{\bar{J}_{g_{\mathrm{O}}} - \bar{J}_{g_{\mathrm{SA}}}}{\bar{J}_{g_{\mathrm{O}}}}\right|, \tag{97}$$

$$\Delta J_h = 100 \left| \frac{\bar{J}_{h_{\mathrm{O}}} - \bar{J}_{h_{\mathrm{SA}}}}{\bar{J}_{h_{\mathrm{O}}}} \right|, \tag{98}$$

$$\Delta \psi_h = \left| \bar{\psi}_{h_{\mathrm{O}}} - \bar{\psi}_{h_{\mathrm{SA}}} \right|, \tag{99}$$

We also directly compare the averaged and non-averaged dynamics. In practice, it would not be convenient to perform the transformation from mean to osculating variables at each time step, either in terms of accuracy or computational time. Thus, we convert the mean Sadov variables coming from the semi-analytical propagation to the angular velocity $\hat{\boldsymbol{w}}_{SA}$ and then compute:

$$\Delta w = \frac{|\bar{w}_{\mathrm{SA}} - w_{\mathrm{O}}|}{w_{\mathrm{O}}}, \quad \begin{bmatrix} \Delta w_x \\ \Delta w_y \\ \Delta w_z \end{bmatrix} = \frac{1}{2} \left| \frac{\bar{\boldsymbol{w}}_{\mathrm{SA}}}{\bar{w}_{\mathrm{SA}}} - \frac{\boldsymbol{w}_{\mathrm{O}}}{w_{\mathrm{O}}} \right|, \tag{100}$$

where $w = |\boldsymbol{w}|$. The quantity Δw is the relative difference in the magnitude of the angular velocity, while Δw_x, Δw_y and Δw_z are differences in the direction cosines of the angular velocity vector. Δw_x, Δw_y and Δw_z are defined so that their maximum value is equal to one. We also compute the rotation that would be required to bring the attitude computed through the semi-analytical propagation to the numerically-computed non-averaged attitude. This rotation angle is defined as:

$$\beta = 2 \arccos \left(\frac{\sqrt{\mathrm{T_r} + 1}}{2} \right), \tag{101}$$

where $\mathrm{T_r}$ is the trace of

$$\mathbf{R}_{\mathrm{SA2O}} = \overline{\mathbf{R}_{\mathrm{i2b_{SA}}}}^{\mathrm{T}} \mathbf{R}_{\mathrm{i2bO}}, \tag{102}$$

with $\mathbf{R}_{\mathrm{i2b}}$ the rotation matrix from $OXYZ$ to $Oxyz$.

In this work, the propagation of both the averaged and non-averaged dynamics is performed using the JULIA's Feagin14 numerical integrator with 1e−13 absolute and relative tolerances.

We study the attitude motion of the triaxial satellite in Fig. 2, whose characteristics are summarised in Table 1, in two cases. In both of them, we first assume that the dynamics of the satellites is affected only by atmospheric drag. In the first case, the satellite is in SAM along an orbit with initial orbital elements

$$a = 7200\,\mathrm{km}, \quad e = 0.01, \quad I = 30\,\mathrm{deg}, \quad \omega = 50\,\mathrm{deg}, \quad \Omega = 120\,\mathrm{deg}, \tag{103}$$

and initial $\boldsymbol{s}$ variables

$$\begin{aligned} \zeta &= 0.9999998116602, \\ J_g &= 280.48\,\frac{\mathrm{kg\,m^2}}{\mathrm{s^2}}, \\ J_h &= 263.54\,\frac{\mathrm{kg\,m^2}}{\mathrm{s^2}}, \\ \psi_l &= 298.62\,\mathrm{deg}, \\ \psi_g &= 71.85\,\mathrm{deg}, \\ \psi_h &= 59.5\,\mathrm{deg}. \end{aligned} \tag{104}$$

In the second case, the satellite is along the same initial orbit (103), but with slightly different initial values of the $\boldsymbol{s}$ variables, i.e.

$$\begin{aligned} \zeta &= 0.9999698989485446, \\ J_g &= 233.78\,\frac{\mathrm{kg\,m^2}}{\mathrm{s^2}}, \\ J_h &= 84.02\,\frac{\mathrm{kg\,m^2}}{\mathrm{s^2}}, \\ \psi_l &= 335.39\,\mathrm{deg}, \\ \psi_g &= 314.64\,\mathrm{deg}, \\ \psi_h &= 149.91\,\mathrm{deg}. \end{aligned} \tag{105}$$

In the first test case the initial rotational kinetic energy is $T_k \sim 10.2044\,\frac{\mathrm{kg\,m^2}}{\mathrm{s}}$, and the parameter μ is equal to $\sim 1.144 \cdot 10^{-5}$. In the second test case, the kinetic energy is smaller and the parameter μ is larger: $T_k \sim 10.2028\,\frac{\mathrm{kg\,m^2}}{\mathrm{s}}$, and $\mu \sim 1.18 \cdot 10^{-3}$. As discussed in Section 4, the quantity μ introduced in (2) can be used to estimate the proximity to the chaotic region in phase space, for which the averaged model is not suitable. Because of the larger value of μ, in the second test case, we expect the initial attitude state to be closer to the chaotic region of the phase space. Furthermore, as the kinetic energy is smaller, we also expect the perturbing effect of atmospheric drag to be more significant. In conclusion, we expect larger errors $(\Delta\zeta, \Delta J_g, \Delta J_h, \Delta\psi_h)$ and larger values of the quantities $(\Delta w, \Delta w_x, \Delta w_y, \Delta w_z, \beta)$ for the second test case than for the first test case.

The results in Table 2 confirm what we expected. The table shows, the maximum values of the errors $(\Delta\zeta, \Delta J_g, \Delta J_h, \Delta\psi_h)$ and the quantities $(\Delta w, \Delta w_x, \Delta w_y, \Delta w_z, \beta)$ obtained over a period of 1 year. For both test cases, when either the low-fidelity model or the mid-fidelity model of the atmospheric drag is employed, the outcomes show that the semi-analytical solution well reproduces the long-term attitude dynamics.

Table 2
Maximum values over the time period $T = 365$ days of the errors $(\Delta\zeta, \Delta J_g, \Delta J_h, \Delta\psi_h)$ and the quantities $(\Delta w, \Delta w_x, \Delta w_y, \Delta w_z, \beta)$ defined in (96)–(101) for the two test cases described in Section 7. The dynamics is assumed affected only by the atmospheric drag perturbation.

Test case	Atmospheric drag model	Outcomes
1	low-fidelity model	$\max_T \Delta\zeta \sim 1.75 \cdot 10^{-9}\%$ $\max_T \Delta J_g \sim 1.2 \cdot 10^{-8}\%$ $\max_T \Delta J_h \sim 2 \cdot 10^{-7}\%$ $\max_T \Delta\psi_h \sim 8 \cdot 10^{-7}$ deg $\max_T \Delta w \sim 1.25 \cdot 10^{-9}$ $\max_T \Delta w_x \sim 4 \cdot 10^{-8}$ $\max_T \Delta w_y \sim 4 \cdot 10^{-8}$ $\max_T \Delta w_z \sim 1.5 \cdot 10^{-10}$ $\max_T \beta \sim 0.001$ deg
1	mid-fidelity model	$\max_T \Delta\zeta \sim 1.75 \cdot 10^{-9}\%$ $\max_T \Delta J_g \sim 1.6 \cdot 10^{-8}\%$ $\max_T \Delta J_h \sim 3 \cdot 10^{-7}\%$ $\max_T \Delta\psi_h \sim 1.2 \cdot 10^{-6}$ deg $\max_T \Delta w \sim 1.25 \cdot 10^{-9}$ $\max_T \Delta w_x \sim 1 \cdot 10^{-7}$ $\max_T \Delta w_y \sim 1 \cdot 10^{-7}$ $\max_T \Delta w_z \sim 1.5 \cdot 10^{-10}$ $\max_T \beta \sim 0.004$ deg
2	low-fidelity model	$\max_T \Delta\zeta \sim 4.3 \cdot 10^{-8}\%$ $\max_T \Delta J_g \sim 7.0 \cdot 10^{-7}\%$ $\max_T \Delta J_h \sim 8 \cdot 10^{-6}\%$ $\max_T \Delta\psi_h \sim 1.5 \cdot 10^{-6}$ deg $\max_T \Delta w \sim 1 \cdot 10^{-7}$ $\max_T \Delta w_x \sim 3 \cdot 10^{-7}$ $\max_T \Delta w_y \sim 4 \cdot 10^{-7}$ $\max_T \Delta w_z \sim 1.5 \cdot 10^{-8}$ $\max_T \beta \sim 0.008$ deg
2	mid-fidelity model	$\max_T \Delta\zeta \sim 4.4 \cdot 10^{-8}\%$ $\max_T \Delta J_g \sim 7.0 \cdot 10^{-7}\%$ $\max_T \Delta J_h \sim 8 \cdot 10^{-6}\%$ $\max_T \Delta\psi_h \sim 2 \cdot 10^{-6}$ deg $\max_T \Delta w \sim 1.2 \cdot 10^{-7}$ $\max_T \Delta w_x \sim 1.5 \cdot 10^{-6}$ $\max_T \Delta w_y \sim 1.5 \cdot 10^{-6}$ $\max_T \Delta w_z \sim 2 \cdot 10^{-8}$ $\max_T \beta \sim 0.006$ deg

The two test cases allow us to compare the two models of the atmospheric drag. It is possible to observe that the error $\Delta\psi_h$ and the quantities $(\Delta w_x, \Delta w_y)$ are larger when the mid-fidelity model is employed. This may be related to the fact that the atmospheric drag perturbation induces a larger average variation of the Sedov variables when the mid-fidelity model is used (see Fig. 3 for the first test case and Fig. 4 for the second test case). When the low-fidelity model is employed the two variables J_h and ψ_h have an almost constant mean value. On the contrary, when the mid-fidelity model is employed, they have a long term variation.

In Fig. 5 and Fig. 6 we show the results of an extended semi-analytical propagation to four years, respectively for the first test case and the second test case. While the mean $\bar{\zeta}$ and $\bar{J}_g$ remain constant with both the low-fidelity model and the mid-fidelity model, the evolution of $\bar{J}_h$ and $\bar{\psi}_h$ differs. The variation arising from the use of the mid-fidelity model does not appear when the low-fidelity model is employed. However, this variation remains small even after four years. Thus, in practical terms, the two models can be deemed to give equivalent results and the choice between them depends on the degree of accuracy desired by the user. Because of the more complex dynamical behaviour, which may affect the evolution of the errors as previously discussed, we selected the mid-fidelity model to perform all the tests described in the remainder of this paper. Table 3 shows a comparison of the computational time between averaged and non-averaged model.

A further test was performed by taking the set up of the first test case and including the effects of gravity-gradient torque, residual magnetic torque, light pressure, lunar and solar gravity, and zonal harmonics J_2, J_3, J_4 and J_5. The averaged model for all these effects was taken from [1]. As expected, the errors $(\Delta\zeta, \Delta J_g, \Delta J_h, \Delta\psi_h)$ and the quantities $(\Delta w, \Delta w_x, \Delta w_y, \Delta w_z, \beta)$ reach significantly larger values (see Figs. 7 and 8). While, $(\Delta w, \Delta w_x, \Delta w_y, \Delta w_z)$ still have acceptable values, β becomes very large after a little time. In fact, β depends on both ψ_l and ψ_g which rapidly diverge from their averaged counterparts. Also, $\Delta\psi_h$ reaches quite large values. As one can observe from Fig. 7, its evolution is a succession of downward-concave parabolas with increasing amplitude, alternated by larger peaks. These peaks are caused by the peculiar evolution of the mean $\bar{\psi}_h$, as one can see in Fig. 9. The figure shows both $\bar{\psi}_{h_{\mathrm{O}}}$ and $\bar{\psi}_{h_{\mathrm{SA}}}$. The two variables display a growing phase shift, to the point when the peaks of one variable correspond to the troughs of the other variable. Nevertheless, the mean evolution of ψ_h is well reproduced, as one can observe from Fig. 10, also showing the evolution of J_h.

Table 3
Computational time to propagate the dynamics over 1 year for the two test cases described in Section 7.

Test case	Atmospheric drag model	Computational time
1	low-fidelity model	non-averaged dynamics propagation: ∼3.2 h semi-analytical propagation: ∼12.03 min
1	mid-fidelity model	non-averaged dynamics propagation: ∼7.5 h semi-analytical propagation: ∼15.13 min
2	low-fidelity model	non-averaged dynamics propagation: ∼3.11 h semi-analytical propagation: ∼13.28 min
2	mid-fidelity model	non-averaged dynamics propagation: ∼7.83 h semi-analytical propagation: ∼16.7 min

Table 4
Characteristics of the axisymmetric satellite in Fig. 13.

Mass	$m = 800$ kg
Moments of inertia	$A = 483.33$ kg m^2, $B = 483.33$ kg m^2 $C = 833.33$ kg m^2
Intrinsic magnetic moment	$\boldsymbol{I}_{\mathrm{m}} = [0.1, 0.1, 0.1]$A m^2
Total reflectivity	bus: 0.6 panel : 0.27
Fraction of the total reflectivity that is specular	bus: 1 panel : 1

The larger values of the errors and the quantities $(\Delta w, \Delta w_x, \Delta w_y, \Delta w_z, \beta)$ shown in this test are mainly caused by the gravity-gradient torque and residual magnetic torque, whose effects are proportional to the inverse of the orbital altitude. Indeed, by increasing the altitude, the maximum values of Δw, Δw_x, Δw_y, Δw_z, β and of the errors $(\Delta\zeta, \Delta J_g, \Delta J_h, \Delta\psi_h)$ over one year decrease. This is shown in Figs. 11 and 12, obtained by changing the initial value of the semi-major to $a = 7658$ km and $a = 8378$ km.

For completeness, we perform a test with the same initial orbit, angular velocity, and attitude of the first test case applied to the axisymmetric satellite in Fig. 13 with characteristics listed in Table 4. For this satellite, the initial modified Sadov variables are:

$$\begin{aligned}
&\zeta = 0.999995327799607,\\
&J_g = 87.27\,\frac{\mathrm{kg\,m^2}}{\mathrm{s^2}},\\
&J_h = 82.02\,\frac{\mathrm{kg\,m^2}}{\mathrm{s^2}},\\
&\psi_l = 296.57\,\mathrm{deg},\\
&\psi_g = 73.76\,\mathrm{deg},\\
&\psi_h = 59.65\,\mathrm{deg}.
\end{aligned} \tag{106}$$

We consider a dynamics affected by the gravity-gradient torque, the residual magnetic torque, the light pressure, the lunar and solar gravity, and the zonal harmonics J_2, J_3, J_4 and J_5, plus the atmospheric drag. The results are reported in Figs. 14 and 15. Also in this case, the error $\Delta\psi_h$ is characterised by large peaks coming from the same phase shift described in the previous test case. Anyway, the trend of the evolution of this mean slow variable is well reproduced as shown by Fig. 16, where it is possible to observe also the evolution of the mean $\bar{J}_h$. The increase of the quantities $(\Delta w_x, \Delta w_y, \Delta w_z)$ and, especially, β is slower than for the triaxial satellites, which highlights the dependence of the accuracy of the averaged model on the characteristics of the object under study.

The results in this paper confirm the findings presented in [1]: β grows faster than the quantities related to the angular velocity, proof that the error tends to increase significantly fast for the fast variables (ψ_l, ψ_g). On the contrary, the mean evolution of the slow variables is typically well reproduced, which implies that we can approximate the evolution of the mean angular momentum expressed in the inertial reference frame with good accuracy.

8. Accuracy maps

The accuracy of the propagation of the averaged model depends two main factors: the magnitude of the atmospheric torques and the rotation speed. Furthermore, the model covers cases where the dynamics is far from any resonance and chaotic region in the phase space. In this section we introduce qualitative accuracy maps to assess the expected accuracy of the propagation of the averaged model over a range of possible initial conditions and perturbing torques. The accuracy maps are defined as

$$\Theta : (\mathcal{M}_{\mathrm{d}}, T_k, \mu) \mapsto \mathcal{E} \tag{107}$$

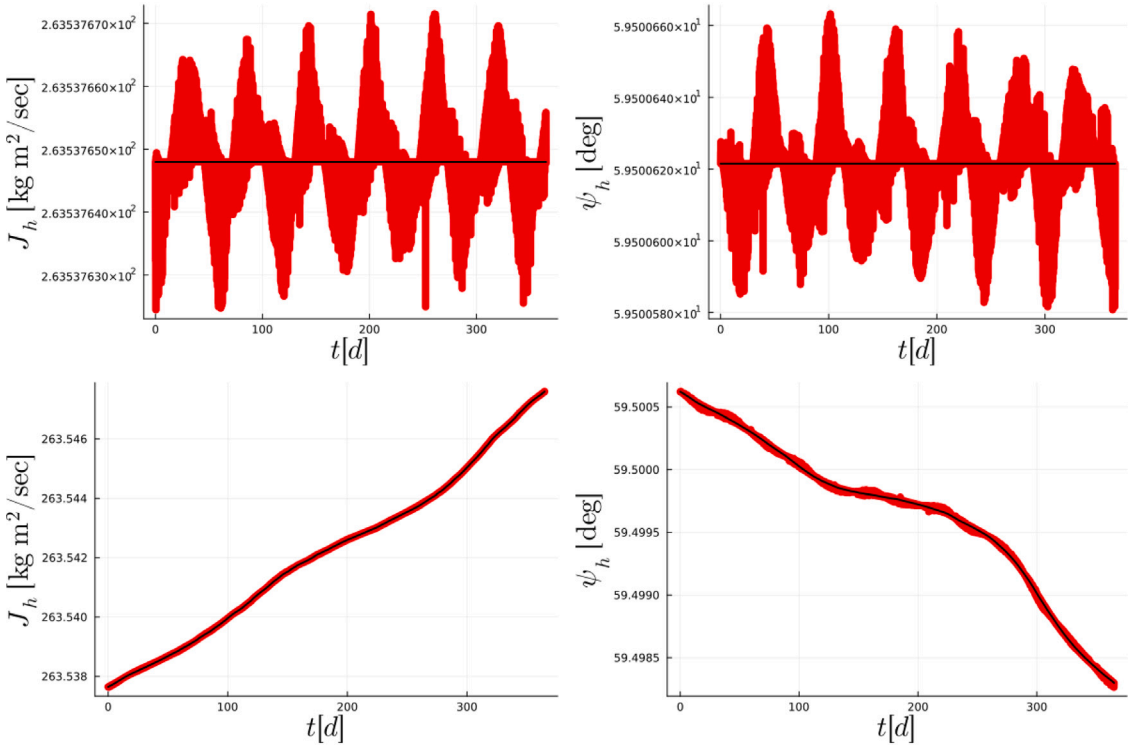

Fig. 3. Evolutions of the mean $\bar{J}_h$ and $\bar{\psi}_h$, computed through the semi-analytical propagation (black), and of J_h and ψ_h (red). Here, we consider the triaxial satellite in Fig. 2 affected by the atmospheric drag perturbation. The top figures are obtained by using the low-fidelity model; the bottom figures are computed by using the mid-fidelity model. The initial conditions are reported in (103) and (104).

where T_k is the initial rotational kinetic energy of the satellite, $\mathcal{M}_\mathrm{d}$ is a quantity used to estimate the magnitude of the atmospheric drag perturbation and

$$\mathcal{E} = \log_{10}\left(\max_{t\in T}\sqrt{\Delta_1^2+\Delta_2^2+\Delta_3^2+\sum_{i=1}^{3}\sum_{j=1}^{3}(\Delta r_{ij})^2}\right), \tag{108}$$

with T the time of propagation,

$$\Delta_1(t) = \frac{p_\mathrm{O}(t)-\bar{p}_\mathrm{SA}(t)}{\sqrt{p_\mathrm{O}^2(t)+q_\mathrm{O}^2(t)+r_\mathrm{O}^2(t)}},$$
$$\Delta_2(t) = \frac{q_\mathrm{O}(t)-\bar{q}_\mathrm{SA}(t)}{\sqrt{p_\mathrm{O}^2(t)+q_\mathrm{O}^2(t)+r_\mathrm{O}^2(t)}},$$
$$\Delta_3(t) = \frac{r_\mathrm{O}(t)-\bar{r}_\mathrm{SA}(t)}{\sqrt{p_\mathrm{O}^2(t)+q_\mathrm{O}^2(t)+r_\mathrm{O}^2(t)}},$$
$$\Delta r_{ij}(t) = r_{ij_\mathrm{O}} - \bar{r}_{ij_\mathrm{SA}},$$

and r_{ij} the elements of the rotation matrix $\mathbf{R}_\mathrm{i2b}$. As previously explained in Section 4, the quantity μ is used as an index of proximity to the chaotic region in the phase space. In line with what was discussed in the previous section, the computation of the maps is performed by adopting the mid-fidelity model. The quantity $\mathcal{M}_\mathrm{d}$ is defined as

$$\mathcal{M}_\mathrm{d} = \max_{\Lambda,\boldsymbol{a}}\left|\sum_{i=1}^{n_f}\boldsymbol{\rho}_i\times\tilde{\boldsymbol{f}}_{\mathrm{d},i}\right| \tag{109}$$

where $\tilde{\boldsymbol{f}}_{\mathrm{d},i}$ is defined in (44) and $\boldsymbol{a}$ is the attitude, which can be more easily described using alternative variables, such as the quaternions or the Euler angles [see 42]. The orbit of the satellite is assumed Keplerian. A propagation time $T = 1$ day is was used to build the maps in this section. Furthermore, for each value of μ we used a (45×25) grid in the $(\mathcal{M}, T_k)$ plane. Fig. 17 shows two examples of maps, one for a small value of μ and one for a large value of μ. The quantity $\mathcal{E}$ is represented with a colour code.

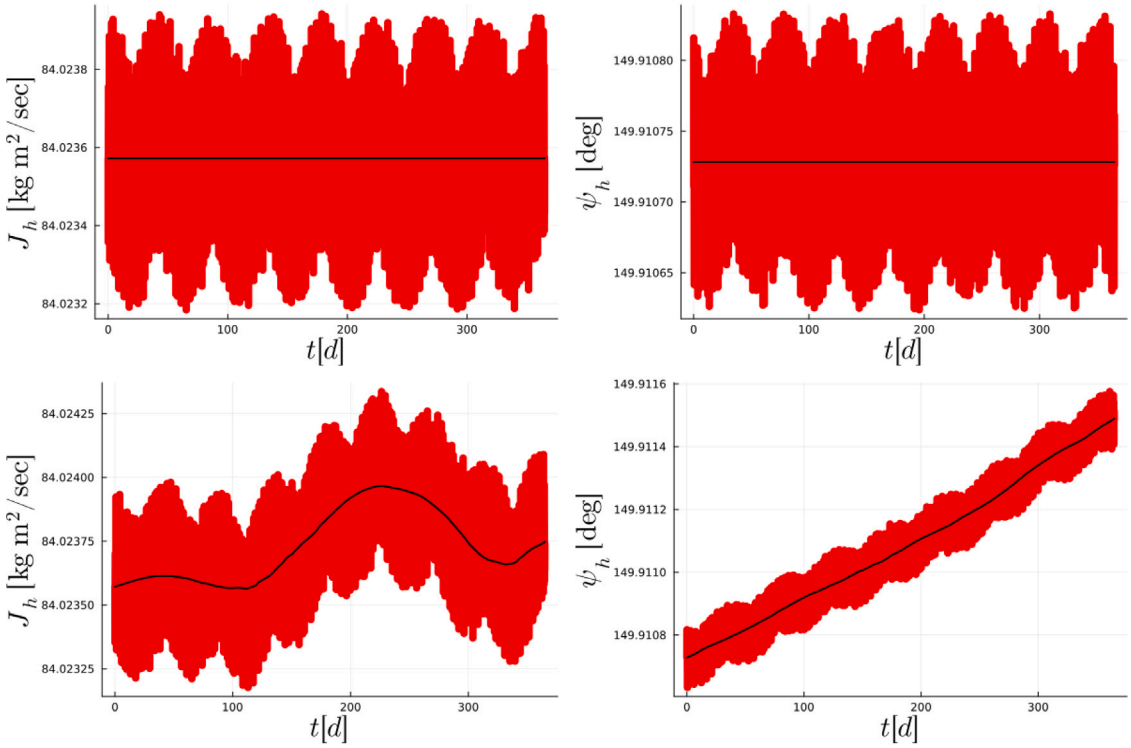

Fig. 4. Evolutions of the mean $\bar{J}_h$ and $\bar{\psi}_h$, computed through the semi-analytical propagation (black) and of J_h and ψ_h (red). Here, we consider the triaxial satellite in Fig. 2 affected by the atmospheric drag perturbation. The top figures are obtained by using the low-fidelity model; the bottom figures are computed by using the mid-fidelity model. The initial conditions are reported in (103) and (105).

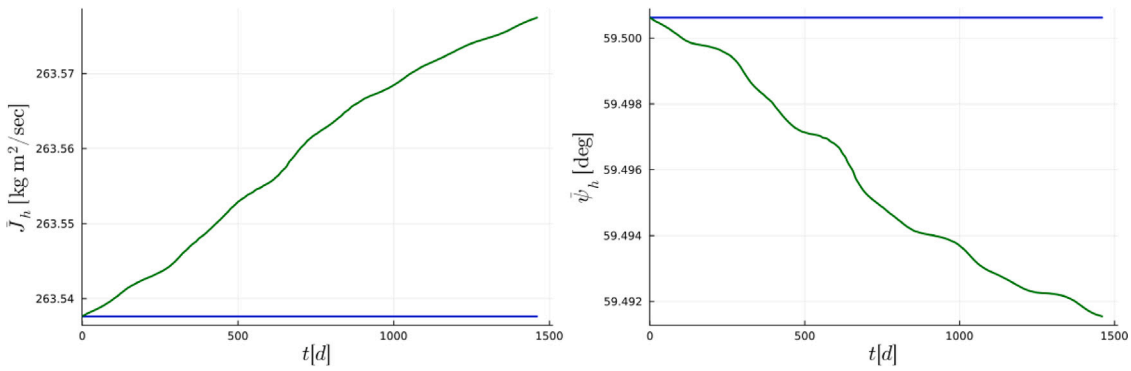

Fig. 5. Evolutions of the mean $\bar{J}_h$ and $\bar{\psi}_h$, computed through the semi-analytical propagation, when the low-fidelity model (blue) and the mid-fidelity model (green) are employed. Here, we consider the triaxial satellite in Fig. 2 affected by the atmospheric drag perturbation. The initial conditions are reported in (103) and (104).

Warmer colours correspond to larger values of $\mathcal{E}$. The value of $\mathcal{E}$ increases at the increase of the size of perturbation and at the decrease of the kinetic energy. Observe also that, as expected, the regularity of the map is partially lost as μ increases.

Since larger values of μ correspond to dynamics progressively approaching the chaotic region of the phase space, the main reason why the regularity of the map is lost is due to the chaoticity of the dynamics. In particular, for $\mu \sim 0.996$, the initial rotational state may already be inside the chaotic region for the larger perturbation values. When the motion is chaotic, it can significantly change for small variations of the initial conditions [see 37].

Note that for each initial condition, the error is expected to increase over integration periods longer than 1 day. However, in the dark blue regions of the maps, we expect that the accuracy of the averaged model is still sufficiently good over a period of 1 year, as shown in the outcomes relative to the single test cases of the previous section when only the atmospheric drag torque is considered as a perturbation.

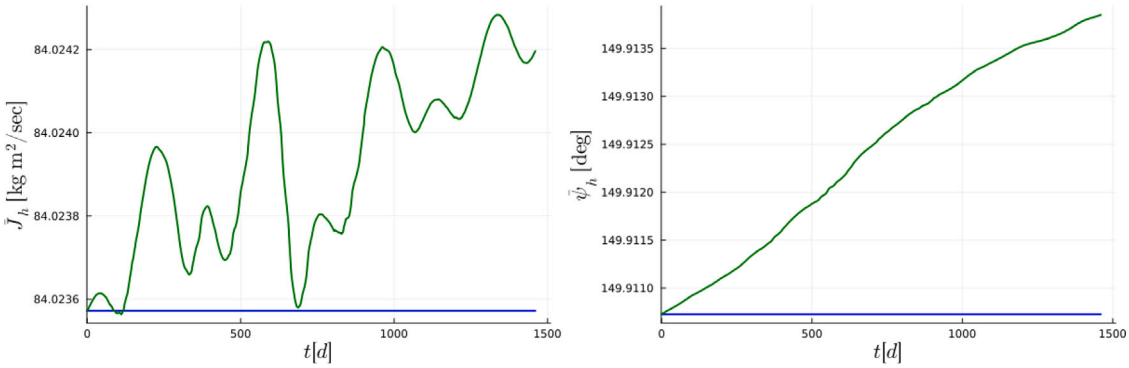

Fig. 6. Evolutions of the mean $\bar{J}_h$ and $\bar{\psi}_h$, computed through the semi-analytical propagation, when the low-fidelity model (blue) and the mid-fidelity model (green) are employed. Here, we consider the triaxial satellite in Fig. 2 affected by the atmospheric drag perturbation. The initial conditions are reported in (103) and (105).

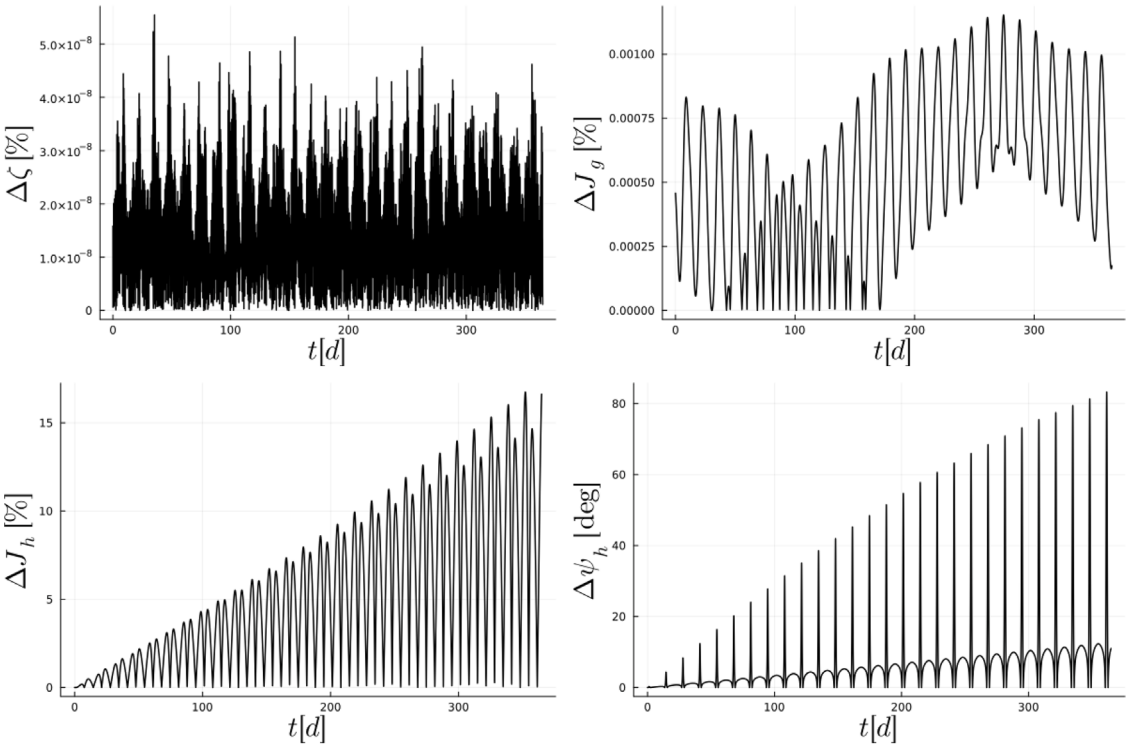

Fig. 7. Evolution of the errors (96)–(99) for the triaxial satellite in Fig. 2 with initial conditions (103), (104). The dynamics is affected by the gravity-gradient torque, the magnetic torque, the light pressure perturbation, the lunar and solar gravity, the zonal harmonics J_2, J_3, J_4 and J_5, besides the atmospheric drag perturbation. The mid-fidelity model is adopted in both the semi-analytical propagation and the numerical averaged procedure.

The average propagation time of the averaged model, over all the initial conditions used to compute the maps, was around ∼19 s, against an average propagation time of the non-averaged model of ∼1 min.

9. Conclusions

This paper presented the development of a first-order averaged model suitable to study the long-term attitude dynamics of Earth-orbiting objects perturbed by atmospheric forces. The model is applicable to both triaxial and axisymmetric objects. It was shown that the technique we proposed to compute the averaged model is general and can be applied to different models of the atmospheric forces. In the paper, we presented two examples: a low-fidelity model and a mid-fidelity model. The main differences between the two force models are in the definition of the dimensionless drag coefficient, the existence of a lift component of the force, and the atmospheric model. Two numerical experiments were performed with different initial values of the attitude variables

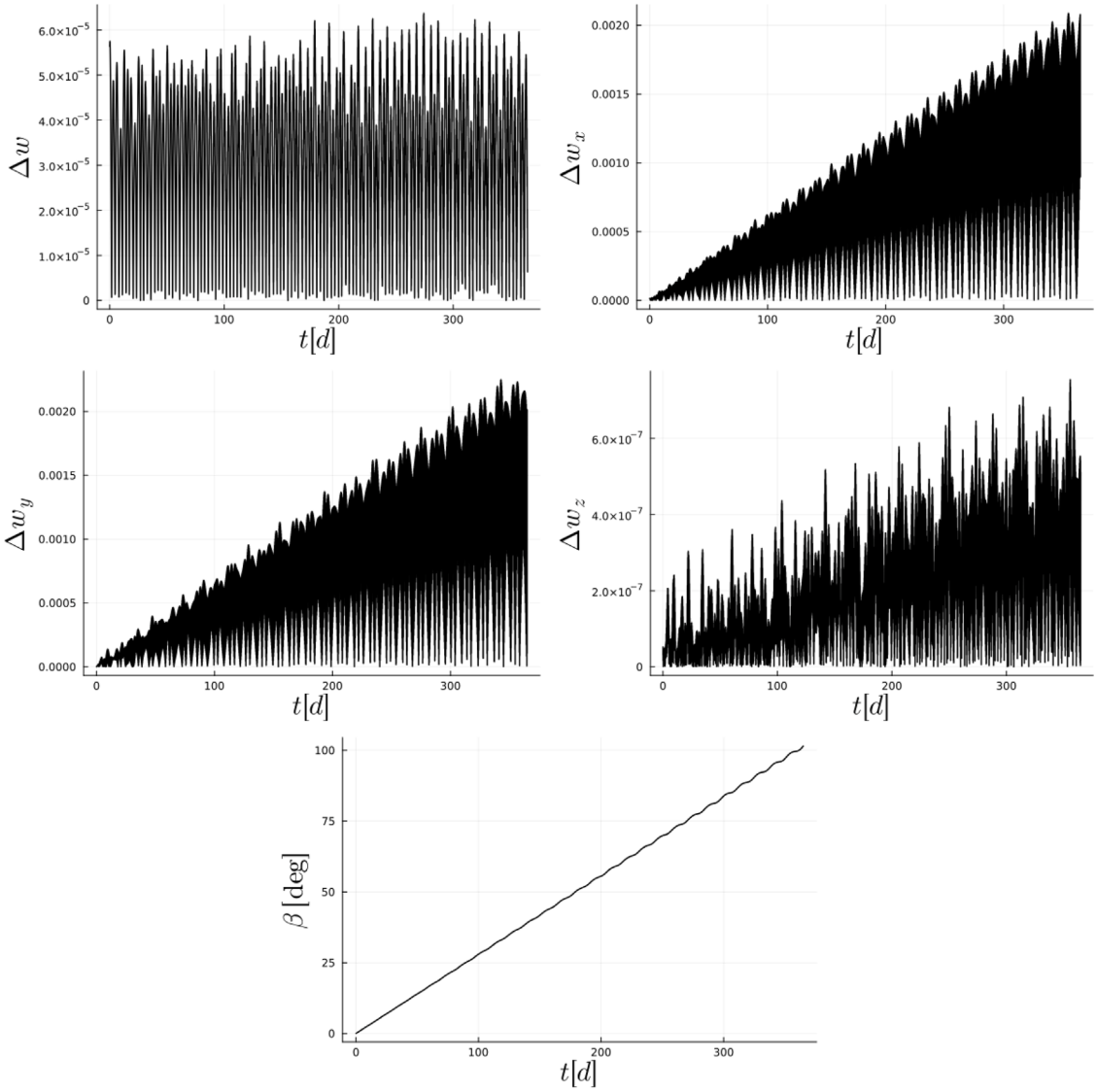

Fig. 8. Evolution of the quantities defined in (100) and (101) for the triaxial satellite in Fig. 2 with initial conditions (103), (104). The dynamics is affected by the gravity-gradient torque, the magnetic torque, the light pressure perturbation, the lunar and solar gravity, the zonal harmonics J_2, J_3, J_4 and J_5, besides the atmospheric drag perturbation. The mid-fidelity model is adopted in both the semi-analytical propagation and the propagation of the full non-averaged dynamics.

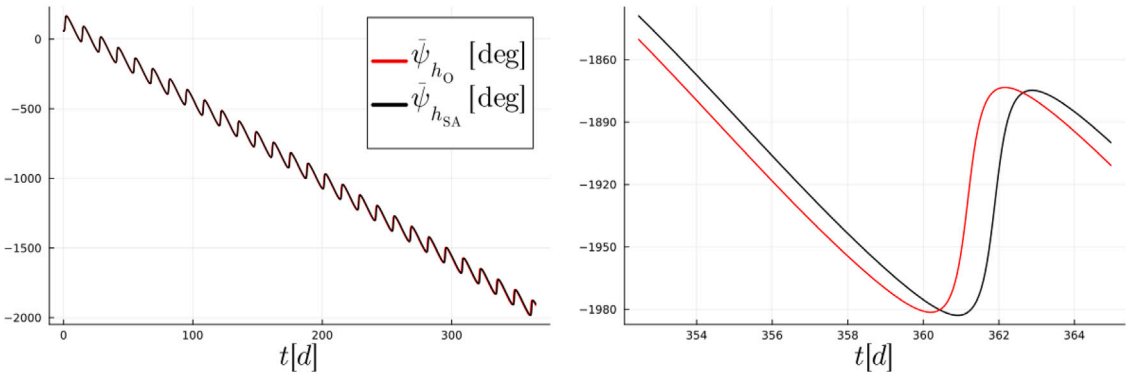

Fig. 9. Evolution of the mean $\bar{\psi}_h$ computed through the numerical procedure (red) and semi-analytically (black).

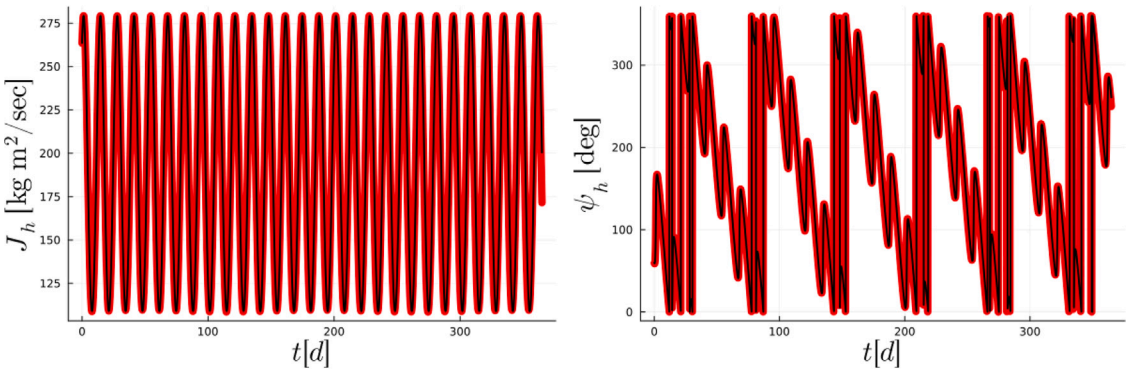

Fig. 10. Evolutions of the mean $\bar{J}_h$ and $\bar{\psi}_h$, computed through the semi-analytical propagation (black) and of J_h and ψ_h (red). Here, we consider the triaxial satellite in Fig. 2 affected by the gravity-gradient torque, the magnetic torque, the light pressure perturbation, the lunar and solar gravity, the zonal harmonics J_2, J_3, J_4 and J_5, besides the atmospheric drag perturbation. The outcomes are obtained by using the mid-fidelity model. The initial conditions are reported in (103) and (104).

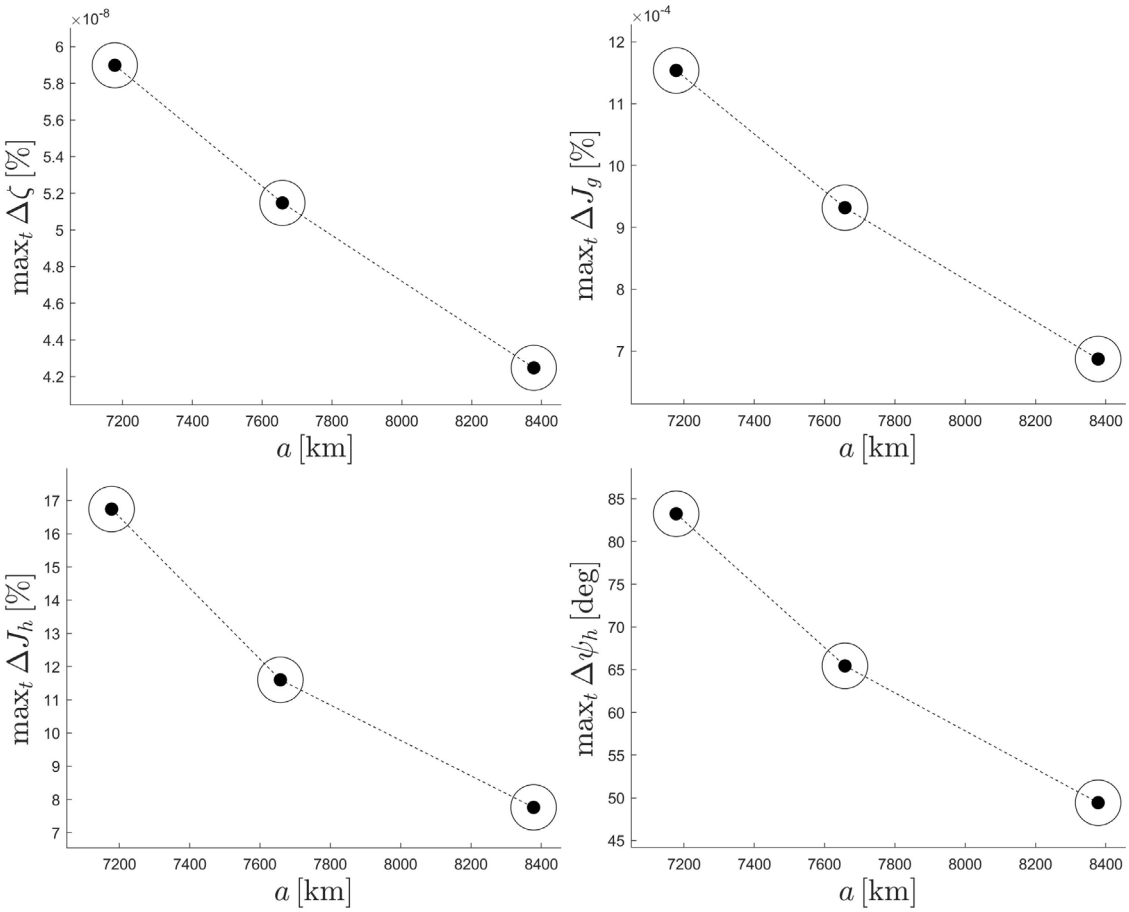

Fig. 11. Maximum values over one year of the errors (96)–(99) at the variation of the initial value of the semi-major axis. The initial attitude conditions are in (104), while the initial eccentricity, inclination, argument of the perigee and right ascension of the ascending node are $e = 0.01$, $I = 30\,\text{deg}$, $\omega = 50\,\text{deg}$ and $\Omega = 120\,\text{deg}$, respectively. The triaxial satellite in Fig. 2 is affected by the gravity-gradient torque, the magnetic torque, the light pressure perturbation, the lunar and solar gravity, the zonal harmonics J_2, J_3, J_4 and J_5, besides the atmospheric drag perturbation. The mid-fidelity model is adopted in both the semi-analytical propagation and the propagation of the full non-averaged dynamics.

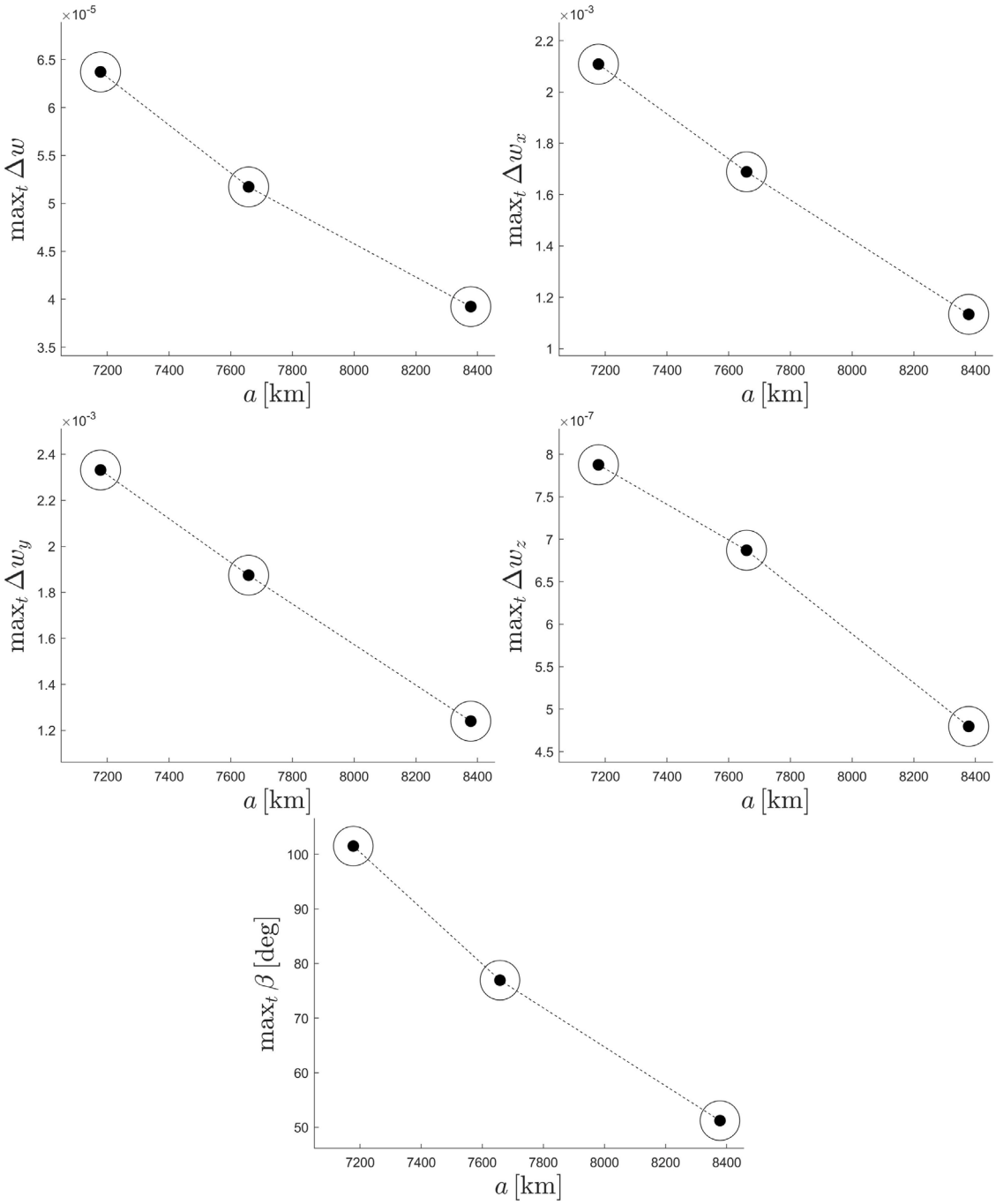

Fig. 12. Maximum values over one year of the quantities defined in (100) and (101) at the variation of the initial value of the semi-major axis. The initial attitude conditions are in (104), while the initial eccentricity, inclination, argument of the perigee and right ascension of the ascending node are $e = 0.01$, $I = 30\,\text{deg}$, $\omega = 50\,\text{deg}$ and $\Omega = 120\,\text{deg}$, respectively. The triaxial satellite in Fig. 2 is affected by the gravity-gradient torque, the magnetic torque, the light pressure perturbation, the lunar and solar gravity, the zonal harmonics J_2, J_3, J_4 and J_5, besides the atmospheric drag perturbation. The mid-fidelity model is adopted in both the semi-analytical propagation and the propagation of the full non-averaged dynamics.

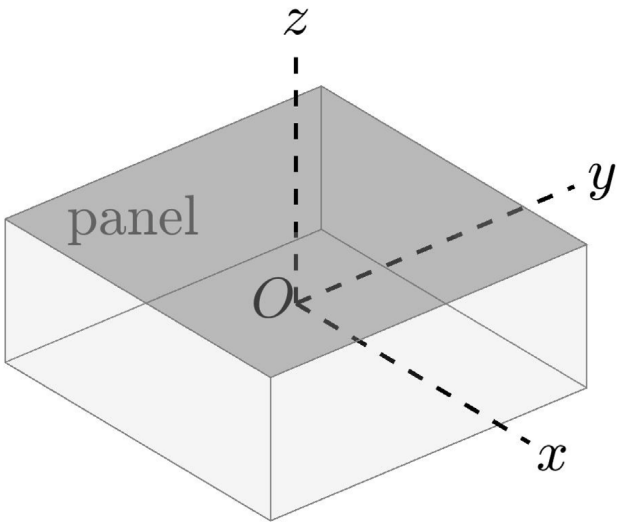

Fig. 13. Axisymmetric satellite.

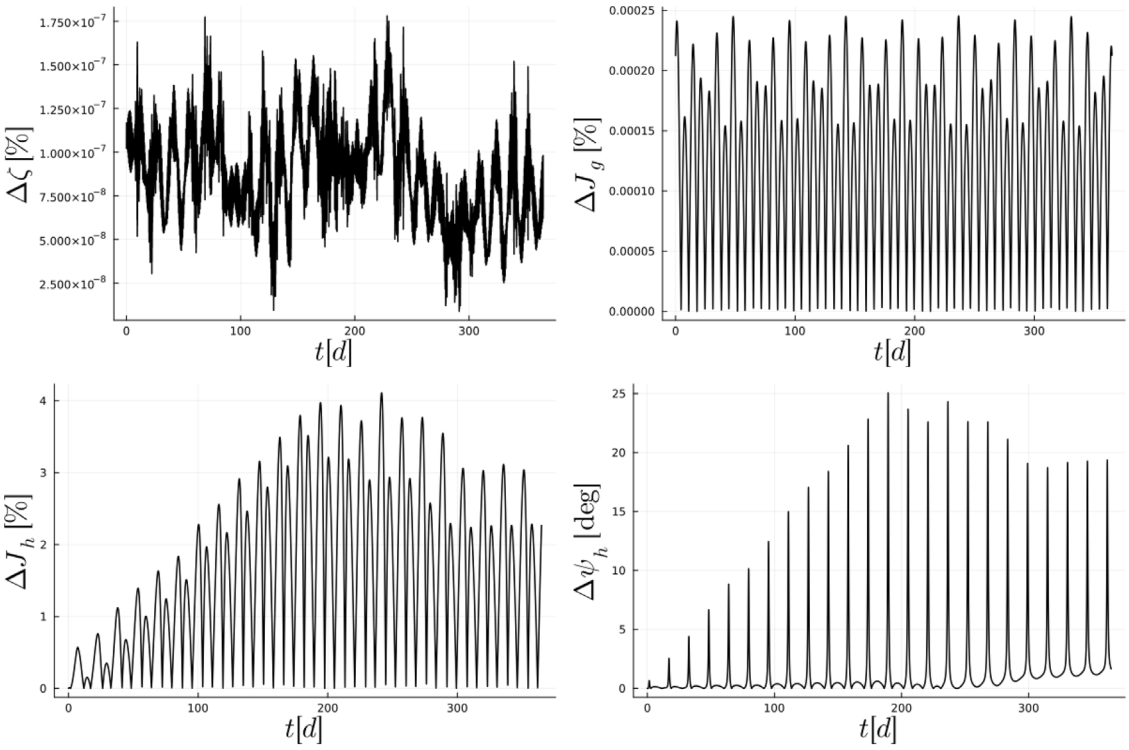

Fig. 14. Evolution of the errors (96)–(99) for the axisymmetric satellite in Fig. 13 with initial conditions (103), (106). The dynamics is affected by the gravity-gradient torque, the magnetic torque, the light pressure perturbation, the lunar and solar gravity, the zonal harmonics J_2, J_3, J_4 and J_5, besides the atmospheric drag perturbation. The mid-fidelity model is adopted in both the semi-analytical propagation and the numerical averaged procedure.

showing that the averaged model, when applicable, can well reproduce the mean evolution of the dynamics. In particular, the results of the averaged propagation of both the low and mid-fidelity model present comparable errors when the attitude dynamics is only affected by aerodynamic forces. These tests were also useful to perform a comparison between the low-fidelity and mid-fidelity model. Indeed, the attitude motion propagated with the mid-fidelity model presents features that do not appear when the low-fidelity model is used instead. Two further numerical experiments were performed by considering additional perturbations. It was shown that when all torques are considered the propagation error can become quite significant over long periods of time, and

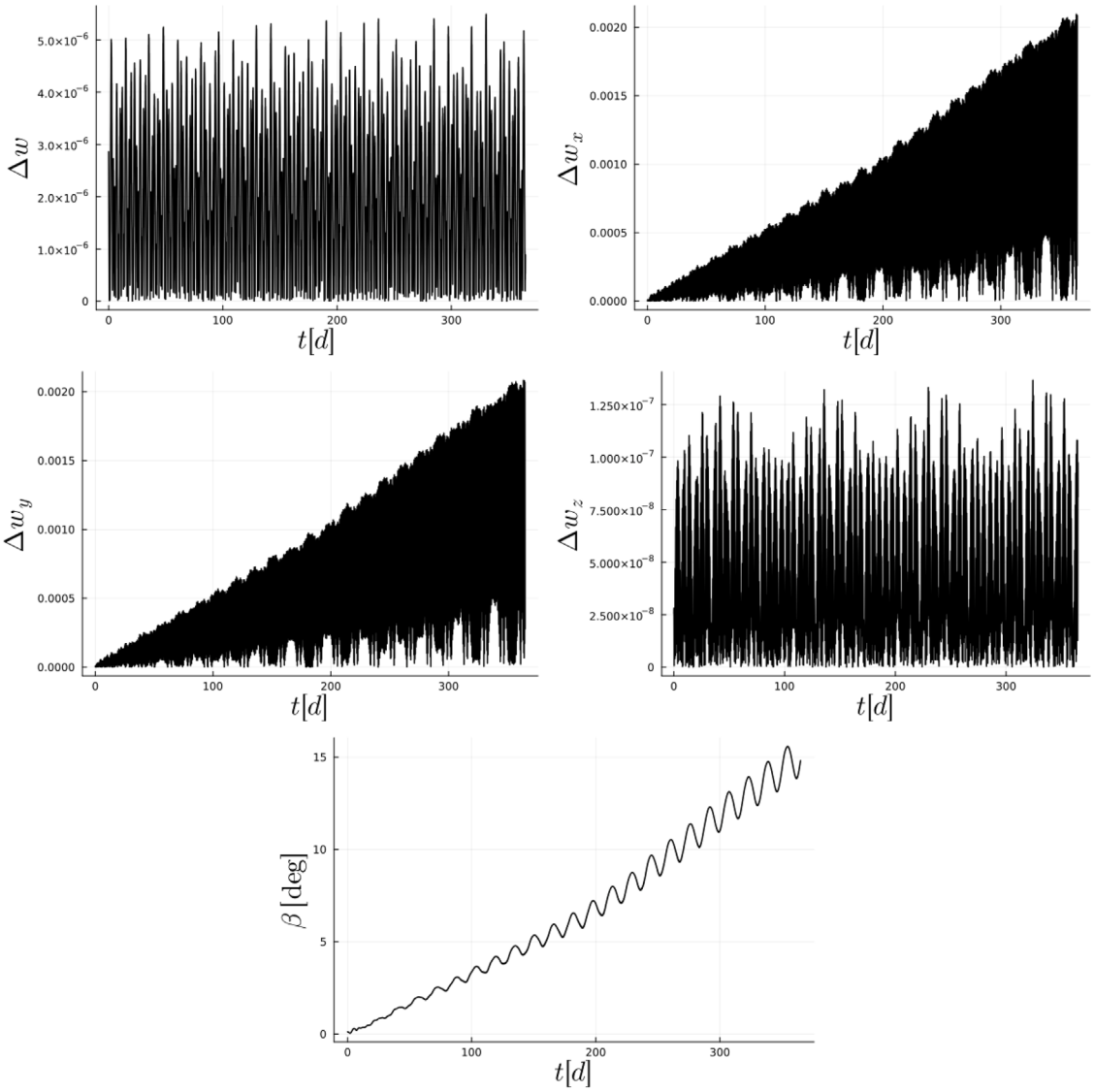

Fig. 15. Evolution of the quantities defined in (100) and (101) for the axisymmetric satellite in Fig. 13 with initial conditions (103), (106). The dynamics is affected by the gravity-gradient torque, the magnetic torque, the light pressure perturbation, the lunar and solar gravity, the zonal harmonics J_2, J_3, J_4 and J_5, besides the atmospheric drag perturbation. The mid-fidelity model is adopted in both the semi-analytical propagation and the propagation of the full non-averaged dynamics.

its maximum value increases at the decrease of the orbital altitude. However, the evolution of the slow variables and the angular velocity is typically accurately reproduced even when the error in the fast angles is large.

An extensive test campaign was performed to assess the accuracy of the averaged model over a range of initial conditions and magnitudes of the perturbing torques. To make the results of this analysis general and applicable to any triaxial satellite, we built maps showing the accuracy of the propagation as a function of the initial kinetic energy, and magnitude of the perturbation. Maps were generated for different values of the index of proximity to the chaotic region of the phase space. It was found that the accuracy decreases for larger perturbations, at the decrease of the initial kinetic energy and at the increase of the proximity to the chaotic region. Finally, over all the cases considered in this paper we found that the average propagation time of the averaged model is about five times smaller than the propagation time of the full non-averaged dynamics.

In the future, it would be interesting to compute higher-order terms to include in the averaged model or develop some corrective methods to increase the attitude accuracy of the semi-analytical solutions. Furthermore, it would also be interesting to treat the rare case of spherical-symmetric satellites with equal principal moments of inertia.

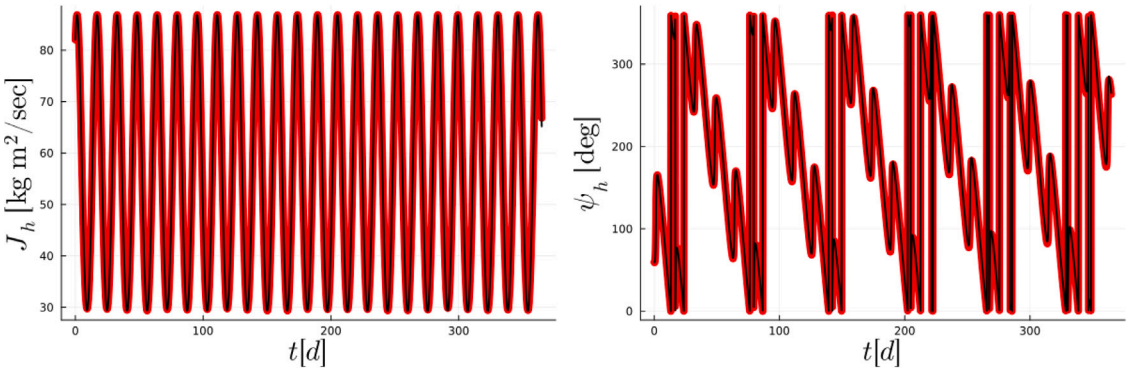

Fig. 16. Evolutions of the mean $\bar{J}_h$ and $\bar{\psi}_h$, computed through the semi-analytical propagation (black) and of the osculating J_h and ψ_h (red). Here, we consider the triaxial satellite in Fig. 13 affected by the gravity-gradient torque, the magnetic torque, the light pressure perturbation, the lunar and solar gravity, the zonal harmonics J_2, J_3, J_4 and J_5, besides the atmospheric drag perturbation. The outcomes are obtained by using the mid-fidelity model. The initial conditions are reported in (103) and (106).

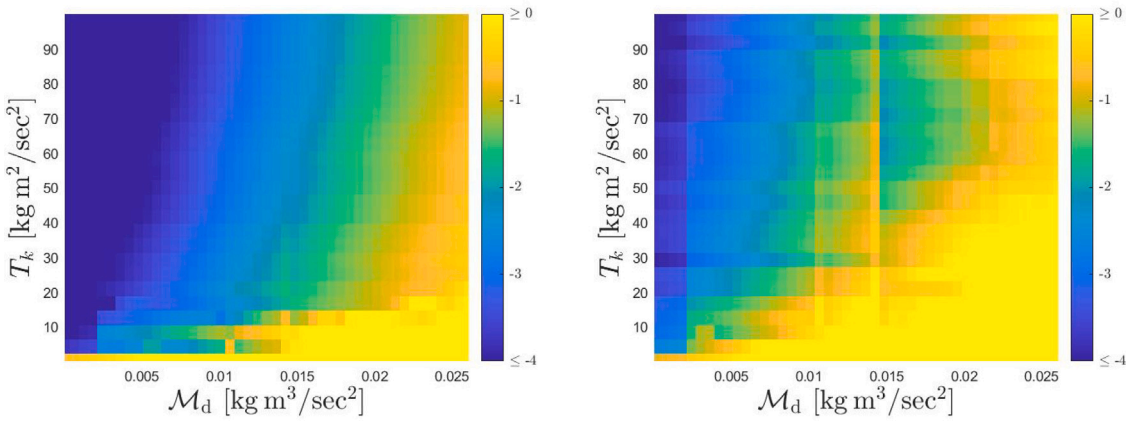

(a) $\mu \sim 0.181$ (b) $\mu \sim 0.996$

Fig. 17. Accuracy maps of the semi-analytical propagation. The quantity defined in (108) is represented with a colour code on the $(\mathcal{M}_d, T_k)$ plane for a fixed value of μ, with $\mathcal{M}_d$ given in (109) and T_k the satellite's kinetic energy.

CRediT authorship contribution statement

I. Cavallari: Writing – original draft, Validation, Software, Methodology, Formal analysis, Conceptualization. **J. Feng:** Writing – review & editing, Supervision, Investigation, Conceptualization. **M. Vasile:** Writing – review & editing, Supervision, Investigation, Funding acquisition, Conceptualization.

Declaration of competing interest

The authors declare the following financial interests/personal relationships which may be considered as potential competing interests: Irene Cavallari reports financial support was provided by European Space Agency, Grant T811-702SD. Jinglang Feng reports financial support was provided by European Space Agency, Grant T811-702SD. Massimiliano Vasile reports financial support was provided by European Space Agency, Grant T811- 702SD. If there are other authors, they declare that they have no known competing financial interests or personal relationships that could have appeared to influence the work reported in this paper.

Acknowledgements

This work was supported through the ESA Contract No. 4000138557/22/D/SR, ITT Semi-Analytic Attitude Propagation Theory - T811-702SD. The authors also acknowledge Ewan Smith, Simão Da Graça Marto for their precious help and collaboration in the project. We would like to thank also the technical officers at the European Space Operations Centre, Jan Siminski and Matteo Losacco for their feedback.

Data availability

Data will be made available on request.

References

[1] Cavallari I, Feng J, Bi S, Vasile M. Semi-analytical attitude propagation for earth orbiting objects. 2024.
[2] Ferrandiz J-M, Sansaturio M-E. Elimination of the nodes when the satellite is a non spherical rigid body. Celest Mech Dyn Astron 1989;46(4):307–20.
[3] Vallejo M. Series de Fourier de functiones elipticas aplicacion a la precesion terrestre (Ph.D. thesis), Ministero de Defensa, Real Instituto y Observatorio de la Armada, Universidad de Zaragoza; 1995.
[4] Elipe A, Vallejo M. On the attitude dynamics of perturbed triaxial rigid bodies. Celest Mech Dyn Astron 2001;81:3–12.
[5] Lara M, Ferrer S. Closed form perturbation solution of a fast rotating triaxial satellite under gravity-gradient torque. Cosm. Res. 2013;51(4):289–303.
[6] Lara M. Complex variables approach to the short-axis-mode rotation of a rigid body. Appl Math Nonlinear Sci 2018;3(2):537–52.
[7] Sidorenko VV. Rotational motion of spacecraft with solar stabilizer. Kosm. Issled. 1992;30(6):780–90.
[8] Zanardi M, Vilhena de Moraes R. Analytical and semi-analytical analysis of an artificial satellite's rotational motion. Celest Mech Dyn Astron 1999;75:227–50.
[9] Celletti A, Sidorenko V. Some properties of the dumbbell satellite attitude dynamics. Celest Mech Dyn Astron 2008;101(1–2):105–26.
[10] Garcia R, Zanardi M, Kuga HK. Spin-stabilized spacecrafts: Analytical attitude propagation using magnetic torques. Math Probl Eng 2009;2009:242396.
[11] Mohmmed M, Ahmed M, Owis A, Diwdar H. Analytical solution of the perturbed oribt-attitude motion of a charged spacecraft in the geomagnetic field. Internat J Adapt Control Signal Process 2013;4:272–86.
[12] Efimov S, Pritykin D, Sidorenko V. Long-term attitude dynamics of space debris in Sun-synchronous orbits: Cassini cycles and chaotic stabilization. Celest Mech Dyn Astron 2018;130(10):62.
[13] Benson C, Scheeres D. Averaged solar torque rotational dynamics for defunct satellites. J Guid Control Dyn 2021;44(4).
[14] Benson C, Scheeres D. Averaged rotational dynamics of GEO debris. In: Flohrer T, Lemmens S, Schmitz F, editors. In: Proceedings of the eighth European conference on space debris, vol. 8, ESA Space Debris Office; 2021.
[15] Zanardi M, Orlando V, Motta GB, Cabette RES. Numerical and analytical approach for the spin-stabilized satellite attitude propagation. In: Proceedings of the 24th international symposium on space flight dynamics. 2015.
[16] Zanardi M, Orlando V, Motta G, Pelosi T, Silva WR. Numerical and analytical approach for the spin-stabilized satellite attitude propagation. Comput Appl Math 2016;35:937–49.
[17] Zanardi M, Celestino C, Motta G, França E, Garcia R. Analysis of analytical attitude propagators for spin-stabilized satellites. Comput Appl Math 2018;37:96–109.
[18] Zanardi MC, Mota V, Borderes-Motta G. Simulations without data updates using analytical attitude propagator GSAM for spin stabilized satellites. J Phys Conf Ser 2019;1365:012020.
[19] Ray V, Scheeres DJ. King-Hele orbit theory for periodic orbit and attitude variations. Mon Not R Astron Soc 2021;501(1):1168–87.
[20] Henrard J. On a perturbation theory using Lie transforms. Celest Mech 1970;3(1):107–20.
[21] Beletsky VV. Motion of an artificial satellite about its center of mass. Nasa technical documents; 1966.
[22] Lips T, Fritsche B, Homeister G, Klinkrad H, Toussaint M. Re-entry risk assessment for launchers - development of the new SCARAB 3.1L. 2007.
[23] Ray V, Scheeres DJ, Hesar SG, Duncan M. A drag coefficient modeling approach using spatial and temporal Fourier expansions for orbit determination. J Astronaut Sci 2020;67(3):1139–68.
[24] Ray V. Advances in atmospheric drag force modeling for satellite orbit prediction and density estimation (Ph.D. thesis), University of Colorado, Boulder, Department of Aerospace and Engineering; 2021.
[25] Sentman L. Free molecule flow theory and its application to the determination of aerodynamic forces. In: LMSC-448514, Lockheed Missiles & Space Company, a division of Lockheed Aircraft Corporation; 1961.
[26] Hancock H. Elliptic integrals. New York J. Wiley; 1917.
[27] Olver FWJ, Lozier DW, Boisvert RF, Clark CW. NIST Handbook of mathematical functions. Cambridge University Press; 2010.
[28] Byrd PF, Friedman M. Handbook of elliptic integrals for engineers and scientists. 2nd Edition. Springer-Verlag New York Berlin Heidelberg; 1971.
[29] Picone JM, Hedin AE, Drob DP, Aikin AC. NRLMSISE-00 empirical model of the atmosphere: Statistical comparisons and scientific issues. J Geophys Res (Space Phys) 2002;107(A12):1468.
[30] Zanardi M, Pereira AJ, Chiaradia J. Spin stabilized satellite's attitude analytical prediction. In: Proceedings of the 22th international symposium on space flight dynamics. 2011.
[31] Vallado DA. Fundamentals of astrodynamics and applications. Space Technology Library; 1997.
[32] Henry IG. Lifetimes of Artificial Satellites of the Earth. Jet Propuls J 1957;27(1):21–4.
[33] Versteeg C, Cotten DL. Preliminary thermal analysis of small satellites. In: Proceedings of the AIAA region II student conference. 2018.
[34] San Juan J, Lopez L, López R. Higher-order analytical attitude propagation of an oblate rigid body under gravity-gradient torque. Math Probl Eng 2012;2012:123138.
[35] Di Carlo M, da Graça Marto S, Vasile M. Extended analytical formulae for the perturbed Keplerian motion under low-thrust acceleration and orbital perturbations. Celest Mech Dyn Astron 2021;133(3):13.
[36] Zuiani F, Vasile M. Extended analytical formulas for the perturbed Keplerian motion under a constant control acceleration. Celest Mech Dyn Astron 2015;121(3):275.
[37] Liu Y, Chen L. Chaos in attitude dynamics of spacecraft. Berlin, Heidelberg: Springer; 2013.
[38] Barrio R, Palaciàn J. Lie transforms for ordinary differential equations: taking advantage of the Hamiltonian form of the perturbation. Int. J Numer Methods Eng 1997;40:2289–300.
[39] Efthymiopoulos C. Canonical perturbation theory, stability and diffusion in Hamiltonian systems: applications in dynamical astronomy. In: Cincotta P, Giordano CM, Efthymiopoulos C, editors. La plata international school on astronomy and geophysics: chaos, diffusion and non-integrability in Hamiltonian systems - applications to astronomy, la plata observatory, July 11-15, 2011. AAA Workshop Series, Asociación Argentina de Astronomía; 2012, p. 3–146.
[40] Di Carlo M, Romero Martin JM, Vasile M. Automatic trajectory planning for low-thrust active removal mission in low-earth orbit. Adv Space Res 2017;59(5):1234–58.
[41] Hughes PC. Spacecraft attitude dynamics. Dover Publications, Inc.; 2004.
[42] Shuster MD. Survey of attitude representations. J Astronaut Sci 1993;41(4):439–517.
[43] Gurfil P, Elipe A, Tangren W, Efroimsky M. The Serret-Andoyer formalism in rigid-body dynamics: I. Symmetries and perturbations. Regul Chaotic Dyn 2007;12(4). 389–425–447.
[44] Bloch A, Gurfil P, Lum KY. The Serret-Andoyer formalism in rigid-body dynamics: II. Geometry, stabilization, and control. Regul Chaotic Dyn 2007;12(4):426–47.